J Electroceram (2011) 26:122–161
DOI 10.1007/s10832-011-9639-6

High-temperature piezoelectric crystals and devices

Holger Fritze

Received: 18 November 2010 / Accepted: 23 March 2011 / Published online: 20 April 2011

Abstract Conventional piezoelectric materials such as quartz are widely used as high precision transducers and sensors based on bulk acoustic waves. However, their operation temperature is limited by the intrinsic materials properties to about 500°C. High-temperature applications are feasible by applying materials that retain their piezoelectric properties up to higher temperatures. Here, langasite ($La_3Ga_5SiO_{14}$) and compounds of the langasite family are the most promising candidates, since they are shown to exhibit bulk acoustic waves up to at least 1400°C. The mass sensitivity of langasite resonators at elevated temperatures is about as high as that of quartz at room temperature. Factors limiting potential use of those crystals include excessive conductive and viscous losses, deviations from stoichiometry and chemical instability. Therefore, the objective of this work is to identify the related microscopic mechanisms, to correlate electromechanical properties and defect chemistry and to improve the stability of the materials by e.g. appropriate dopants. Further application examples such as resonant gas sensors are given to demonstrate the capabilities of high-temperature stable piezoelectric materials. The electromechanical properties of langasite are determined and described by a one-dimensional physical model. Key properties relevant for stable operation of resonators are found to be shear modulus, density, electrical conductivity and effective viscosity. In order to quantify their impact on frequency and damping, a generalized Sauerbrey equation is given. Mass and charge transport in single crystalline langasite are correlated with langasite's defect chemistry and electromechanical properties. First of all, the dominant charge carriers are identified. Undoped langasite shows predominant ionic conduction at elevated temperatures. As long as the atmosphere is nearly hydrogen-free, the transport is governed by oxygen movement. A dominant role of hydrogen is observed in hydrogenous atmospheres since the diffusion coefficient of hydrogen is orders of magnitude higher than that of oxygen. The loss in langasite is found to be governed up to about 650°C by viscoelastic damping related to the above mentioned movement of oxygen ions. Donor doping is shown to lower the loss contribution. Above 650°C the impact of the conductivity related loss becomes pronounced. Here, lowering the conductivity results generally in decreased losses. The evaluation of langasite's applicability is focused on mapping the regimes of gas insensitive operation. The most relevant feature with respect to frequency fluctuations of resonator devices is the formation of oxygen vacancies. In nominally hydrogen free atmospheres the calculated frequency shift becomes pronounced below oxygen partial pressures of 10^{-17}, 10^{-24} and 10^{-36} bar at 1000, 800 and 600°C, respectively. Water vapor is found to shift the resonance frequency at higher oxygen partial pressures. In the hydrogen containing atmospheres applied here, langasite can be regarded as a stable resonator material above 10^{-13} bar and 10^{-20} bar at 800 and 600°C, respectively. The incorporation of OH-groups determines the frequency shift.

Keywords Langasite · Piezoelectric transducers · High temperature

H. Fritze (✉)
Institute of Energy Research and Physical Technologies,
Clausthal University of Technology, Am Stollen 19,
38640 Goslar, Germany
e-mail: holger.fritze@tu-clausthal.de

1 Introduction

1.1 High-temperature piezoelectric materials

High-temperature piezoelectric devices open a wide range of new applications due to the option to realize advanced operation principles. Related examples include high-temperature surface acoustic wave devices which can be interrogated remotely [1, 2] or the in-situ monitoring of high-temperature processes using the ability of piezoelectric resonators to determine gas composition and temperature dependent mechanical and electrical properties of sensor films [3]. Beyond that anticipated applications of resonant sensors include the deposition rate monitoring during chemical vapor deposition and thermogravimetry on small volumes. Thus, operating temperatures considerably above 500°C are often required.

Stable long-term operation of piezoelectric devices at high temperatures causes demands on the materials which exceed those of room-temperature applications significantly. Basic requirements include the absence of phase transformations and low damping of mechanical movements or oscillations at high temperatures. As a consequence, conventional piezoelectric materials such as α-quartz (α-SiO_2) and non-stoichiometric lithium niobate ($LiNbO_3$) are not suited for high-temperature applications. Quartz undergoes a destructive phase transformation at 573°C [4]. In practice, the maximum temperature of about 450°C is determined by high losses [5]. Nonstoichiometric lithium niobate and lithium tetraborate ($Li_2B_4O_7$) either decompose at 300°C or exhibit phase transformations at 500°C, respectively [6–9].

Polycrystalline materials can be generally excluded from further discussions due to their low Curie temperature, high electrical conductivity and grain boundary related damping. The highest theoretical limits given by the Curie temperature are 490°C for lead titanate (perovskite structure: $PbTiO_3$), 685°C for bismuth titanate (Aurivillius phase: $Bi_4Ti_3O_{12}$) or 940°C for bismuth titanium niobate (double perovskite structure: Bi_3TiNbO_9). Analogously, the operation of strontium niobate ($Sr_2Nb_2O_7$) is limited by its melting point at 1700°C. In practice much lower limits apply due to losses caused by low electrical conductivity. Many of those materials become extrinsic semiconductors. Further, scattering of the acoustic waves at grain boundaries (or pores) causes high losses [6].

Further requirements include the stability in oxidizing or reducing atmospheres, i.e. the formation of oxides or the (partial) reduction of the materials is not tolerable. Aluminium nitride (AlN) can be, in principle, used up to 1150°C. However, poor oxidation resistance and the lack of sufficiently large crystals prevent its use [10–13].

Langasite ($La_3Ga_5SiO_{14}$), its isomorphs and gallium phosphate ($GaPO_4$) are promising candidates for high-temperature applications. They enable operation temperatures significantly above 500°C. The ultimate temperature limits are given by the melting point of langasite and the phase transition of $GaPO_4$ at 1470 [14, 15] and 970°C [16–18], respectively. Another important aspect focussing the interest on langasite is the availability of high quality and large size single crystals manufactured by the Czochralski technique [14, 15, 19]. $GaPO_4$ is, in principle, very attractive since shows extremely low losses [20–22]. However, productivity and yield of growing $GaPO_4$ single crystals is rather low. Extremely anisotropic growth rates, twinning and the incorporation of OH-groups in the crystals are observed [23–26]. Due to those difficulties the availability of $GaPO_4$ is limited which prevents its large scale application.

Recently, oxyborate single crystals ($ReCa_4O(BO_3)_3$, Re: rare earth element) has been developed. They do not show phase transformations up to its melting point at about 1500°C and are, therefore, promising materials for high-temperature operation. Most remarkably, those crystals exhibit very low conductivity, for example 5×10^{-7} S/m at 800°C [27–29] which is about one and three orders of magnitude lower than that for $GaPO_4$ and langasite, respectively. As a consequence, the loss is very low which results in resonant devices with exceptional high resonator quality factors even at 900°C. Currently, a maximum operation temperature of 1000°C is reported for $GdCa_4O(BO_3)_3$. Above that the thin film platinum electrodes used here degrade strongly [28]. However, higher operation temperatures are expected.

Table 1 lists piezoelectric materials of practical relevance and their operation temperature limits. Further materials of the langasite-related family of compositions are not given since langasite is regarded as the model representative.

Langasite has been demonstrated to be operational as bulk acoustic device up to temperatures close to its melting point at 1473°C [32]. This fact motivates the objective of this work to explore its materials properties in detail. For comparison, data of $GaPO_4$ and α-quartz are included.

1.2 Langasite

The first compound of the langasite-related family of compositions was discovered at Moscow State University in 1979 [33]. Since then the material attracted

Table 1 Operation temperature limits of single crystalline piezoelectric materials

Material	Temperature limit [°C]	Remarks	Reference
$Li_2B_4O_7$	230	Excessive ionic conductivity	[6]
$LiNbO_3$	300	Decomposition	[6–9]
$LiTaO_3$	300	Decomposition	[6]
α-quartz	573	Phase transformation	[4, 5]
$AlPO_4$	588	Phase transformation	[6, 20, 30]
$GaPO_4$	970	Phase transformation	[16–18, 31]
AlN	~1000	Oxidation resistance	[10–13]
Langasite	1470	Melting point	[14, 15, 32]
Oxyborates	~1500	Melting point	[27–29]

significant attention for improved electronic oscillators and filters. Advantages of langasite over α-quartz include higher piezoelectric coupling which results in higher resonator quality factors, and thus in reduced phase noise [34–36]. A couple years had to pass before the interest turned on langasite's high-temperature properties [37–39]. The literature in those days did not contain meaningful data about the high-temperature properties of langasite [6]. In particular, the option to operate langasite as Bulk Acoustic Wave (BAW) resonator at high temperatures was under question. The latter was caused by the lack of conductivity data and of the knowledge about their impact on the resonance behavior. In 1999, langasite BAW resonators could be operated up to 750°C [40]. Increasing experience in data acquisition and electrode preparation enabled the demonstration of even higher operation temperatures such as 900°C in 2000 [41, 42] and more than 1400°C in 2005 [32]. Figure 1 demonstrates the appearance of BAW's in langasite at extremely high temperatures by showing the temperature dependent resonance frequency. The data are normalized using the room temperature resonance frequency f_{RT} and compared with that of $GaPO_4$ and α-quartz.

Langasite belongs to the structure type of the trigonal calcium gallium germanate $Ca_3Ga_2Ge_4O_{14}$ as visualized in Fig. 2. Due to the presence of four distinct cation sites according to $A_3BC_3D_2O_{14}$, the langasite structure is very complex and allows, therefore, several substitutions. In this regard, langasite is particularly suited as model compound since nearly every size cation can be accommodated on one of its four different cation sites [33]. Layers of vertice-connected C- and D-tetrahedra alternate with layers of A-site Thomson cubes and B-octahedra. A special feature of the langasite structure is the appearance of gallium in the differently coordinated B- and C-sites [43]. The corresponding ions, oxygen coordination numbers and ionic radii are shown in Table 2.

Appropriate growth conditions have to be chosen to suppress microstructural defects. Nowadays, large and high quality crystals can be grown [15, 19, 45, 46]. Beyond that, the composition of the melt determines the properties of the crystals. Two issues have to be regarded. First and most obviously, the stoichiometry and the purity of the oxide mixture used for the Czochralski growth impacts the defect chemistry. Secondly, the growth process itself impacts the melt composition.

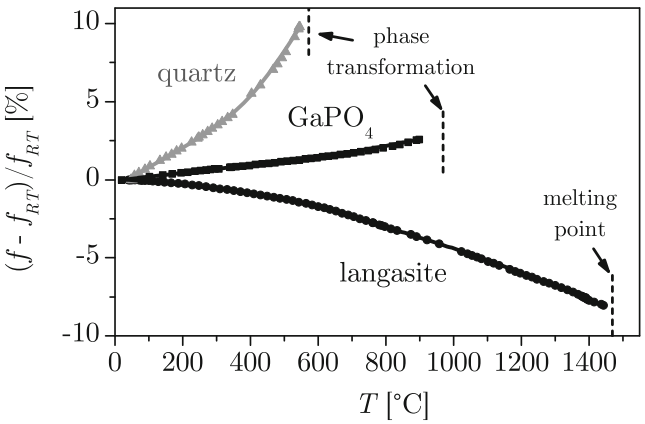

Fig. 1 Temperature dependent resonance frequency of langasite, gallium phosphate and quartz BAW resonators

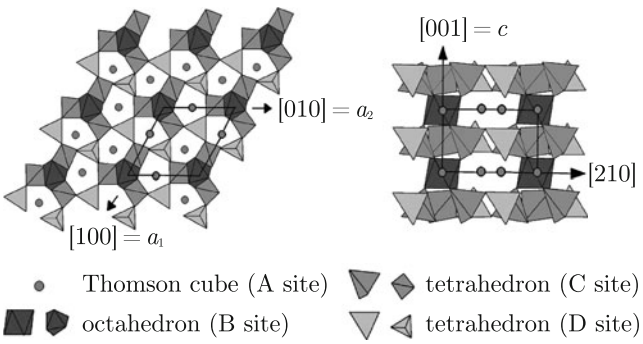

Fig. 2 $Ca_3Ga_2Ge_4O_{14}$-type crystal structure [33]

Table 2 Sites and oxygen coordination of the cations in langasite as well as ionic radii of the cations [44]

Site	A	B	C	D	
Occupation	La^{3+}	Ga^{3+}	Ga^{3+}	50% Ga^{3+}	50% Si^{4+}
Oxygen coordination	8	6	4	4	
Ionic radii [10^{-10} m]	1.16	0.62	0.47	0.47	0.26

Here, crucial factors are the segregation coefficients and the mass ratio of crystal and melt. Stoichiometry derivations of the melt composition are commonly compensated by the formation of either cation or anion vacancies [39, 47]. For example, the activation energy of the electrical conductivity varies depending on the position where the specimen is taken from the crystal boule (seed end, central part, tail end) by up to about 0.1 eV [39]. The fact underlines that even samples from the same crystal boule exhibit significant differences in their properties. The situation might be even worth if crystals of different size or purchased samples are compared. Here, the mass ratio of crystal and melt and the position in the crystal are under question. In order to exclude the latter problems to some extend, crystals from a single manufacturer (IKZ Berlin, see Appendix A) are used predominantly.

1.3 Research objectives

Specific demands on the piezoelectric materials are defined by anticipated applications such as resonant microbalances. Those devices correlate very small mass changes during film deposition onto resonators or gas composition dependent stoichiometry changes of thin films already deposited onto the resonators with their resonance frequency [48, 49]. Thereby, specific surface affinity layers allow chemical sensing. For example, changes in mass equivalent to submonolayers of oxygen atoms can be detected which enables the stoichiometry determination of surface oxides [50]. Consequently, the mass or density of those piezoelectric transducers must be environmental independent to insure high mass resolution. In other words, the minimization of stoichiometry changes is essential to ensure stable resonance frequencies. In this context the detailed understanding of the defect chemistry is required.

Further, atomistic mechanisms which cause excessive conductive and viscous damping must be understood. Thus, the kinetic mechanisms controlling electronic and ionic transport in the piezoelectric materials must be investigated at high temperatures. Those insights might motivate the application of certain dopants to decrease e.g. losses or to minimize environmental dependent stoichiometry variations.

The evaluation of the application limits of high-temperature piezoelectric devices must include the detailed determination of the temperature dependent electromechanical properties such as piezoelectric coefficients, elastic constants and viscosity. However, those issues are not in the main focus of this article. Those properties are presented in detail elsewhere [3] and summarized in Section 2. Thereby, special emphasis is put on the identification of the most relevant materials properties for stable operation at high temperatures.

The work is focussed exclusively on BAW resonators since they can be operated using robust electrode structures. Thus, the electrodes are not the limiting components while determining the properties of the piezoelectric crystals at extremely high temperatures. In contrast, common SAW devices require rather tiny electrode structures whose limited thermal stability prevents reliable measurements.

2 Electromechanical properties

2.1 Thickness shear mode resonators

The piezoelectric materials langasite, gallium phosphate and α-quartz belong to the same crystal class and point group, namely the trigonal system and 32, respectively. Therefore, their electromechanical properties can be described by a single physical model. In particular, approaches known for α-quartz can be reviewed and modified for resonators operated at high temperatures.

Unless specified otherwise the resonators used here are plane-parallel disks where the axis normal to the surface is oriented in the x_2-direction according to Fig. 3 (y-cut[1]). The electric field is applied in the x_2 direction which results in a mechanical displacement in the x_1 direction as shown schematically in Fig. 4 [3]. In other words, the piezoelectric plate undergoes a shear deformation across its thickness. The corresponding vibration mode is called thickness shear mode (TSM).

[1]The crystal cut designation follows [51].

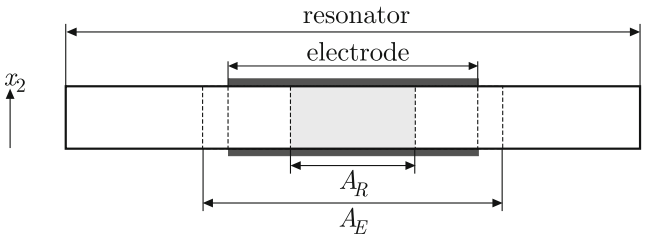

Fig. 3 Cross section of a circular TSM resonator showing the electrodes and the extent of the characteristic areas A_R and A_E (see text) which lie in the x_1–x_3 plane

The electromechanical properties mechanical stiffness c_R, piezoelectric e_R and dielectric constant ε_R as well as physical properties such as the mechanical stress are tensors of different order. The inherent tensor notation can be transformed into a compressed matrix notation since the symmetry of the crystals reduces the number of non-zero tensor components drastically. The independent materials constants for the y-cut resonators are reduced to $c_R = c_{66}$, $e_R = e_{26} = -e_{11}$ and $\varepsilon_R = \varepsilon_{22} = \varepsilon_{11}$. The approach is described in detail in [51–53].

2.2 Losses in piezoelectric resonators

Factors which affect the loss in piezoelectric resonators include [53, 54]

- Resonator design and manufacturing such as resonator blank geometry (contour, dimensional ratios), electrode geometry, surface finish,
- Operation conditions such as mounting stresses, drive level, overtone number, viscosity of the surrounding medium and
- Intrinsic properties of the resonator material such as electronic and ionic transport, interstitial diffusion, motion of dislocations.

The resonator design and manufacturing as well as the operation conditions must meet certain standards to insure proper operation of the resonators. These requirements are well known and excessively published for quartz under room temperature conditions, e.g.:

- Flat or plano-plano resonators with a diameter to thickness ratio greater than 50 usually provide acceptable performance if they are operated in the fundamental mode [55].
- The diameter of the electrodes should be generally smaller than 40% of the resonator diameter.
- The separation of unwanted spurious modes from the resonance frequency can be achieved by limiting the diameter of electrodes as function of the resonator thickness as described in [56].

The resonators used here follow essentially these standards and show low losses at room temperature.

Since the resonators shall be operated at high-temperatures, material related losses are expected to be dominant. To include these losses, the above mentioned electromechanical properties have to be, in general, treated as complex quantities. The imaginary parts $\omega\eta_R$ and σ_R/ω in

$$\hat{c}_R = c_R + \hat{e}_R^2/\hat{\varepsilon}_R + j\omega\eta_R \quad \text{and} \quad \hat{\varepsilon}_R = \varepsilon_R - j\sigma_R/\omega \tag{1}$$

stand for the mechanical and dielectric loss, respectively [53, 57].[2] Thereby, η_R and σ_R represent the effective viscosity and the electrical conductivity of the resonator, respectively. It should be noted that the mechanical and dielectric losses are related by the complex dielectric constant $\hat{\varepsilon}_R$ included in the piezoelectrically stiffened shear modulus $\hat{c}_R$. The fact reflects the piezoelectric coupling which causes a depolarization field. The latter is affected by dissipation effects of mobile charge carriers [53]. The complex piezoelectric constant is given by

$$\hat{e}_R = e_R + j\epsilon_R. \tag{2}$$

Thereby, the name of the imaginary part ϵ_R is not specified since there is no simple physical interpretation. Irrespective of its origin, ϵ_R can be seen as phase lag between the electrical and mechanical properties. Microscopic explanations are e.g. the jumping of lattice defects or the movement of domain walls in polycrystalline materials [58, 59]. However, for most materials systems ϵ_R can be set to zero [53]. The validity of this

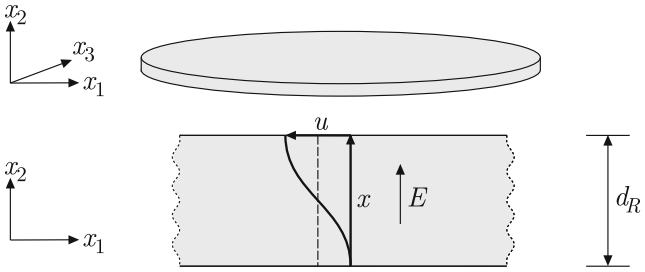

Fig. 4 Orientation and displacement of the TSM resonators used here

[2] In [57] the electromechanical coupling $K^2 = \varepsilon^2/(ec)$ is considered instead of ε.

approximation for the materials of interest in this work is demonstrated in [3]. Nevertheless, ϵ_R is included into to the set of equations in order to evaluate its impact on the resonance behavior. If applies, films are described in analogy to Eq. 1 by $\hat{c}_F = c_F + j\omega\eta_F$ with η_F as viscosity of the film.

The overall loss can be expressed by the resonator quality factor Q (Q-factor) as given at the end of Section 2.4. The Q-factor is determined from the bandwidth Δf_S at half maximum of the conductance peak $G_{\max}/2$ and the series resonance frequency f_S according to $Q = f_S/\Delta f_S$ [53, 60].

2.3 Modeling of the electromechanical properties

The electrical impedance $Z = Z' + jZ''$ or admittance $Y = G + jB = 1/Z$ of a coated TSM resonator can be calculated using a set of constitutive equations which includes linear piezoelectric equations, Newton's equation of motion and Maxwell's equations. Without electrical losses the approach is state of the art and can be found in textbooks [52, 53, 61]. A complete analytical solution of the one-dimensional physical model reflecting all types of material related losses is presented in [3] and results in case of a single film on each side of the resonator in the electrical impedance $\widetilde{Z}$

$$\widetilde{Z} = \frac{d_R}{j\omega A_R\,\hat{\varepsilon}_R}\left(1-\frac{K^2\left(\zeta_{F_1}+\zeta_{F_2}+2\tan\frac{\alpha_R}{2}\right)}{\alpha_R\left(1-\zeta_{F_1}\zeta_{F_2}+\left(\zeta_{F_1}+\zeta_{F_2}\right)\cot\alpha_R\right)}\right). \tag{3}$$

Thereby, the abbreviations $K^2 = \hat{e}_R^2/(\hat{\varepsilon}_R\hat{c}_R)$ for the electromechanical coupling coefficient of the resonator material, $\zeta_{Fn} = \sqrt{\rho_{Fn}\hat{c}_{Fn}}/\sqrt{\rho_R\hat{c}_R}\tan\alpha_{Fn}$ for the normalized acoustic load impedance of the front and rear film (index $n = 1$ and 2), $\alpha_R = \omega d_R\sqrt{\rho_R/\hat{c}_R}$ and $\alpha_{Fn} = \omega d_{Fn}\sqrt{\rho_{Fn}/\hat{c}_{Fn}}$ for the acoustic phase shift inside the resonator and the films, respectively, are used. The density and the angular frequency are expressed by ρ and ω, respectively. The tilde indicates intermediate results which refer temporarily to the area A_R. The final expressions are given in Section 2.5.

2.4 Electrical equivalent circuit

For the further discussion $\widetilde{Z}$ is interpreted as a parallel arrangement of the motional impedance Z_M and static impedance $\widetilde{Z}_S$

$$1/\widetilde{Z} = 1/Z_M + 1/\widetilde{Z}_S \tag{4}$$

with

$$Z_M = \frac{d_R}{j\omega A_R\hat{\varepsilon}_R}\left(\frac{\alpha_R(1-\zeta_1\zeta_2+(\zeta_1+\zeta_2)\cot\alpha_R)}{K^2\left(\zeta_1+\zeta_2+2\tan\frac{\alpha_R}{2}\right)}-1\right) \tag{5}$$

and

$$\widetilde{Z}_S = \frac{d_R}{j\omega A_R\hat{\varepsilon}_R}. \tag{6}$$

$\widetilde{Z}_S$ is the static impedance and represents the bulk properties of the resonator. The fact becomes obvious by expanding the complex dielectric constant $\hat{\varepsilon}_R$ leading to a parallel arrangement of the static capacitance $\widetilde{C}_S$ and resistance $\widetilde{R}_S$

$$1/\widetilde{Z}_S = j\omega\widetilde{C}_S + 1/\widetilde{R}_S \tag{7}$$

with

$$\widetilde{C}_S = \varepsilon_R\,A_R/d_R \tag{8}$$

and

$$\widetilde{R}_S = 1/\sigma_R\;d_R/A_R \tag{9}$$

The corresponding equivalent circuit is visualized in Fig. 5(a). For completeness, a lead resistance R_L and a stray capacitance C_L have to be added. These elements reflect predominantly the properties of the sample holder. Actual measurements are performed using a calibrated setup consisting of network analyzer and sample holder. Therefore, R_L and C_S essentially vanish.

Further, the motional impedance Z_M remains to be evaluated. Its transformation and approximations leading to the extended Butterworth–van Dyke equivalent

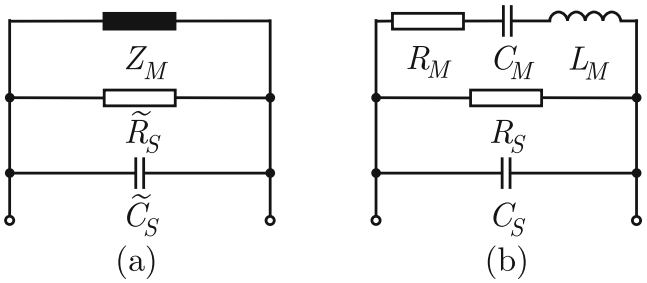

Fig. 5 Equivalent circuit for the resonator (**a**) and extended Butterworth-van Dyke equivalent circuit (**b**)

circuit according to Fig. 5(b) are described in [3]. Here, the result for an uncoated resonator

$$R_M = \underbrace{\frac{N^2\pi^2 d_R}{8A_R {e_R}^2}\,\eta_R}_{R_\eta} + \underbrace{\frac{\left(N^2\pi^2-8\right)d_R\sigma_R}{8A_R\left(\varepsilon_R{}^2\omega^2+\sigma_R{}^2\right)}}_{R_\sigma}, \tag{10}$$

$$C_M = \frac{8A_R}{d_R}\,\frac{e_R^2\varepsilon_R}{N^2\pi^2\left(e_R^2+c_{66}\varepsilon_R\right)-8e_R^2} \tag{11}$$

and

$$L_M = \frac{d_R}{8A_R}\,\frac{d_R^2\rho_R}{e_R^2} \tag{12}$$

is given, only. The intermediate steps are of minor relevance for the further discussion.

It have be noted that R_M represents losses and can be interpreted as series of R_η and R_σ. The physical property therein expected to exhibit the strongest temperature dependence is used as index. The limits of R_σ for $\sigma \to 0$ and $\sigma \to \infty$ vanish. The maximum in between is found at the so-called dielectric relaxation frequency $\omega_\varepsilon = \sigma_R/\varepsilon_R$.

The elements of the equivalent circuit can be used to express the total loss in form of the Q-factor which follows from the ratio of stored E_S and dissipated energy E_D multiplied by 2π according to [62]

$$Q = 2\pi\frac{E_S}{E_D} = \sqrt{\frac{L_M}{C_M}}\,\frac{1}{R_M}\,\frac{R_S}{R_S+R_M} = Q_0\frac{R_S}{R_S+R_M}. \tag{13}$$

The quality factor Q_0 represents highly resistive resonator materials, i.e. the low-temperature case.

The figure of merit used here for the resonant structures is the Qf-product since it enables to compare devices showing different frequencies.

2.5 Effective resonator area

The calculation of the electrical impedance Z for a finite resonator device requires the introduction of the area A_R. However, the one-dimensional physical model describes a resonator of infinite dimensions in the x_1–x_3 plane which results in a constant amplitude of mechanical vibration u_1 for a given value of x_2. In contrast, finite and, in particular, partially electroded resonators exhibit a distribution of their amplitude in the x_1–x_3 plane which can be approximated by a Gaussian function [63]

$$u_1(x_1) = u_1^{\max}\, e^{-w\,{x_1}^2}. \tag{14}$$

Thereby, w and $u_1^{\max}$ stand for the width and the maximum of the distribution, respectively. As a consequence, the one-dimensional model is applicable to finite devices provided that the problem of the conflictive amplitude distribution can be solved. For that purpose, the approach chosen here is to replace the area showing the amplitude distribution by an effective area of constant amplitude.

Within the one-dimensional model, the effective area corresponds to the already introduced property A_R. Measured values of A_R are substantially smaller than the effective electrode area A_E. Their ratio is found to be $A_R/A_E \approx 0.4\ldots0.7$ [3]. The difference between the areas can be explained qualitatively by comparing the distributions of the mechanical amplitude and of the electrical field which determine the effective values of A_R and A_E, respectively:

- The amplitude of the mechanical vibration at the border of the electrode u_1^b with respect to the maximum at the center of the electrode $u_1^{\max}$ is small, e.g. $u_1^b/u_1^{\max} = 0.08$ for typical TSM resonators [63]. The amplitude distribution depends on the mass of the electrodes. Even gold electrodes[3] of only 25 nm lead to $u_1^b/u_1^m = 0.4$ [64]. Therefore, the average amplitude is always smaller than the maximum amplitude. The fact can be described by an effective area A_R which is smaller than the geometrical area of the electrode.
- The distribution of the electrical field is largely homogenous. There is a minor impact of fringing fields, only. According to calculations by finite element analysis the effective electrode area A_E is 5–10% larger than the geometrical electrode area.

So far, the static impedance $\widetilde{Z}_S$ refers to A_R. Consequently, the property does not reflect the effective electrode area A_E of finite resonators. The required modification can be achieved by replacing A_R with A_E in Eqs. 6–9 leading to the capacitance $C_S = \varepsilon_R A_E/d_R$ and the resistance $R_S = 1/\sigma_R\, d_R/A_E$. Thus, the impedance of the resonator device follows in analogy to Eq. 4 from

$$1/Z = 1/Z_M + 1/Z_S = 1/Z_M + j\omega C_S + 1/R_S. \tag{15}$$

The distinction of effective resonator area and the effective electrode area is not necessarily required at or

[3] The situation is comparable to platinum electrodes applied here since their density is similar.

near room temperature where the resonators are highly resistive. Under such circumstances

- The static resistance R_S does not appear in common models and
- The part of the static capacitance which is related to the difference $A_E - A_R$ can be assigned to the stray capacitance C_L.

Despite the inconsistency regarding the static capacitance, common models describe the experimental results satisfactorily. However, problems arise as soon as the static resistance and capacitance get changed due to e.g. high operation temperatures.

2.6 High-temperature materials data

The bulk properties of the piezoelectric crystals are extracted from impedance spectra at frequencies far below the resonance frequency of the samples. In contrast, the electromechanical properties are determined by fitting the solution of the one-dimensional physical model to the resonance spectra $Z(f)$. The fit procedure is presented in [3]. The description of the experiments and initial values for the fit procedure are given in Appendix B. The dashed lines in the plots for σ_R and η_R represent data used for the parameter study in Section 2.7.

Figure 6 shows the bulk conductivity σ_R of the materials of interest as function of temperature. Most remarkably, the values of langasite are more than two orders of magnitude higher than those of $GaPO_4$ and quartz. Therefore, the impact of the conductivity on the resonance spectra is expected to play a pronounced role in case of langasite resonators.

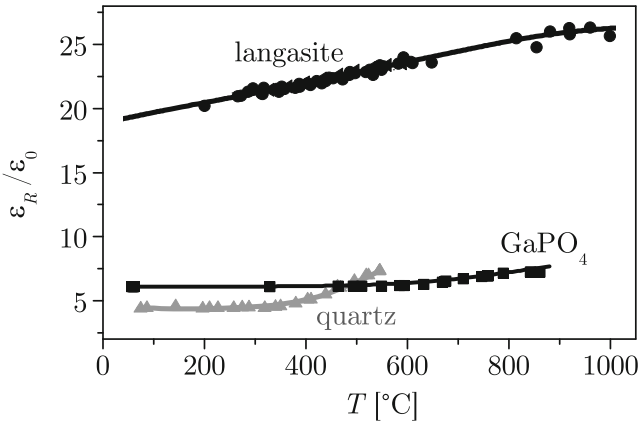

Fig. 7 Temperature dependent dielectric constant of langasite, gallium phosphate and quartz

The temperature dependence of dielectric constants ε_R is given in Fig. 7. The value for langasite is in accordance with literature data measured up to about 350°C [33]. This comparison cannot be done for $GaPO_4$ since high-temperature data are obviously not published.

The shear modulus c_R is presented in Fig. 8. Its temperature dependence determines predominantly the course of the resonance frequency as is becomes obvious by comparing Figs. 1 and 8. A modified presentation of the shear modulus according to $(c_{66} - c_{RT})/c_{RT}$ matches the pattern of $(f - f_{RT})/f_{RT}$ in Fig. 1. The relative change in the respective entire temperature range are the smallest for $GaPO_4$ (5%). Stronger changes are found for langasite and quartz (9 and 17%, respectively). The values presented here are in reasonable

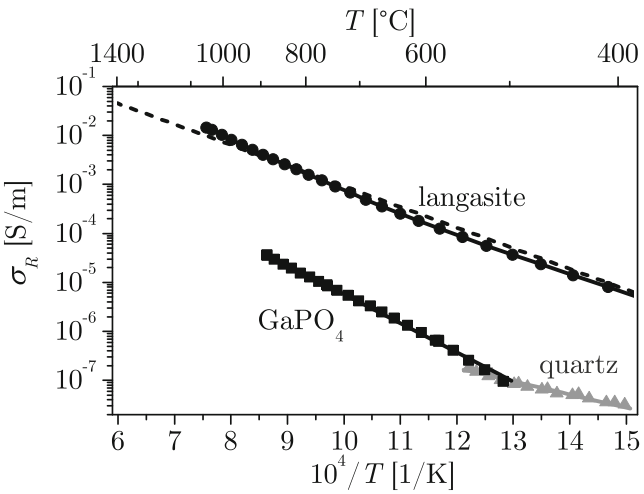

Fig. 6 Arrhenius plot of the conductivity of langasite, gallium phosphate and quartz

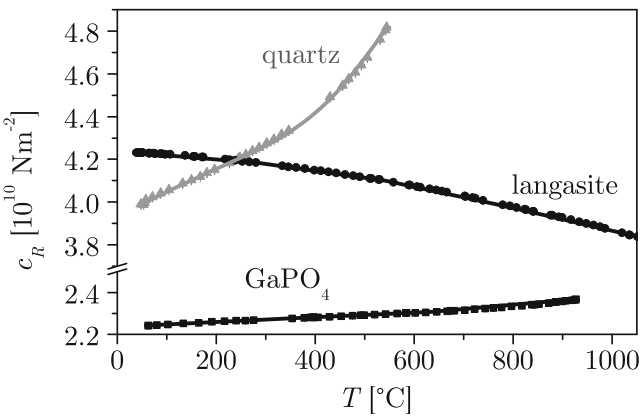

Fig. 8 Temperature dependent shear modulus of langasite, gallium phosphate and quartz

agreement with literature data determined e.g. by resonant ultrasound spectroscopy up to 450°C [65, 66].

Figure 9 shows the temperature dependent piezoelectric coefficient e_R. Since its sign does not impact the dynamic behavior of TSM resonators, its modulus is of interest for the further discussion. Remarkably, the piezoelectric coefficient of langasite is about three times as large as that of quartz. Further, the property is expected to decrease with increasing temperature as observed for $GaPO_4$ and quartz. In contrast, langasite shows a reverse temperature dependence which might be an intrinsic piezoelectric property. In any case, the large value and its increase with increasing temperature are advantageous features of langasite for high-temperature applications. Another important issue is the very little temperature dependence of the piezoelectric coefficient of $GaPO_4$. At 930°C, the modulus is only 5% lower than that at room temperature. The results for $GaPO_4$ matches very well the data from the crystal's manufacturer measured at temperatures up to about 700°C by the Michelson interferometry [67, 68]. The piezoelectric coefficient of langasite correspond to data given up to 500°C in [38]. Further, independent measurements performed in our laboratory [69, 70] are in accordance with these data.

The viscosity of the piezoelectric materials exhibits a quite different behavior as presented in Fig. 10. $GaPO_4$ and quartz show an almost linear slope in the $\log(\eta_R) - T$ plot. The only exception is found in a narrow temperature range around 400°C where the resonance spectra of the quartz resonators cannot be fitted due to numerous spurious resonances. Explanations for this behavior can be found in [71, 72]. In contrast, langasite undergoes some loss maximus as seen by the shallow peaks of the viscosity at about 250, 700 and 950°C.

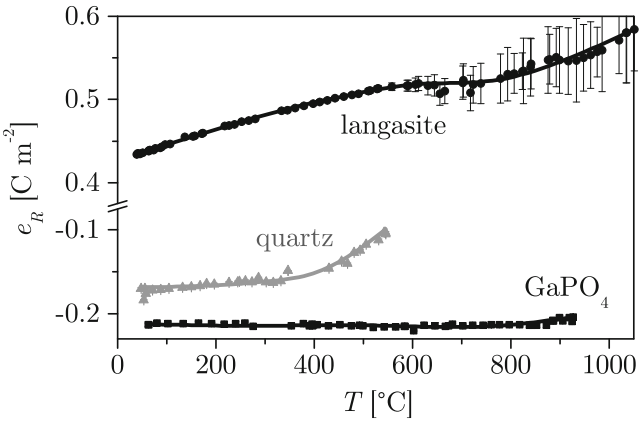

Fig. 9 Temperature dependent piezoelectric constant of langasite, gallium phosphate and quartz

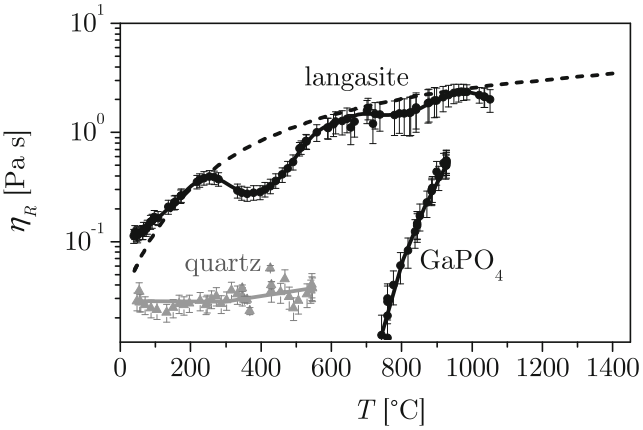

Fig. 10 Temperature dependent viscosity of langasite, gallium phosphate and quartz

Remarkably, the loss tends to decrease with increasing temperature above 950°C.

2.7 Crucial resonator properties

Crucial properties with respect to high-temperature operation of the resonators must be identified. For that purpose, the impact of the physical properties on the resonance frequency and the resonator quality factor is calculated.

The materials data used for the following parameter study correspond largely to those of langasite. They are extrapolated to 1400°C in order to extend the calculations to extremely high temperatures which are not experimentally accessible because of the limited stability of the thin film electrodes applied here. Further, single activation energies for the conductivity σ_R and the viscosity η_R are assumed. Those data are indicated by dashed lines in Figs. 6 and 10. Details about the materials data and the dimensions of the resonators used here are summarized in Appendix B.

The first part of the parameter study focusses on the series resonance frequency f_S which is calculated from Eq. 15 using the condition to $Im(Z) = 0$. Numerical values are obtained with a accuracy of 10^{-6} Hz. Further, the derivatives of these frequencies $\partial f_S / \partial [..]$ for all parameters [..] being included in the physical model are calculated and multiplied by $[..]/f_S$. The approach results in relative values of the derivatives $\kappa_{[..]}$

$$\kappa_{[..]} = \frac{[..]}{f_S}\frac{\partial f_S}{\partial [..]} = \frac{[..]}{f_S}\frac{\Delta f_S}{\Delta [..]} \tag{16}$$

which enables their comparison. The right hand side of Eq. 16 is written using small differences in order to

relate relative changes of the frequency to that of the parameters [..] by $\kappa_{[..]}$

$$\frac{\Delta f_S}{f_S} = \kappa_{[..]} \frac{\Delta[..]}{[..]}. \tag{17}$$

The meaning of Eq. 17 becomes obvious taking the thickness of the resonator as example, i.e. $[..] = d_R$. Its change Δd_R can be related to a mass change Δm by $\Delta d_R/d_R = \Delta m/m$ which results in

$$\frac{\Delta f_S}{f_S} = \kappa_{d_R} \frac{\Delta m}{m}. \tag{18}$$

Since the numerical calculation yields $\kappa_{d_R} = -1$, the example corresponds to the Sauerbrey equation [64]

$$\frac{\Delta f_S}{f_S} = -\frac{\Delta m}{m} \tag{19}$$

which is the first order approach to relate relative changes in mass and frequency. In general, Eq. 17 can be regarded as a kind of generalized Sauerbrey equation for the corresponding physical property or dimension of the resonator.

Figure 11 shows values for $\kappa_{[..]}$ calculated from the series resonance frequency f_S. The signs of the changes are indicated in the plot. This calculation is performed for langasite, $GaPO_4$ and quartz at room temperature. Obviously, these piezoelectric materials exhibit a similar behavior. The impact of the resonator properties on the series resonance frequency can be summarized as follows:

- Changes in thickness d_R, shear modulus c_{66} and density ρ_R influence f_S predominantly.
- The piezoelectric coefficient e_R and the dielectric constant ε_R show a little impact, only.
- The effective resonator area A_R, the effective electrode area A_E, the viscosity η_R and the conductivity σ_R do not affect f_S at room temperature.

The influence of the film properties on the piezoelectric resonators made of different materials is also similar.

- Changes in thickness d_F and density ρ_F dominate.
- The shear modulus c_F and the viscosity η_F does not affect f_S under the conditions chosen here.

Finally, it should be noted that the stray capacitance C_L and the lead resistance R_L do not impact f_S. This fact is the reason why f_S is commonly determined while operating resonant sensors.

The most important issue in the context of this work concerns the relative frequency shift at elevated temperatures which is calculated taking langasite as example. Thereby, special attention has to be drawn to loss related properties, i.e. η_R and σ_R. Figure 12 shows remarkable features for changes in f_S at 500 and 1000°C:

- The impact of the conductivity σ_R becomes pronounced at 1000°C.
- The sign of the relative deviation of ε_R changes going from 500 to 1000°C.
- The effect of the film properties remains almost unchanged.

So far, relative derivatives of the frequency are calculated and compared. If the focus is drawn exclusively on the resonator, d_R, c_{66} and ρ_R cause the strongest impact. In order to identify the dominant parameters for absolute frequency changes according to $\Delta[..]\partial f_S/\partial[..]$, the magnitude of environmentally dependent variations of the corresponding parameter $\Delta[..]$ must be considered. Thereby, the temperature is expected to

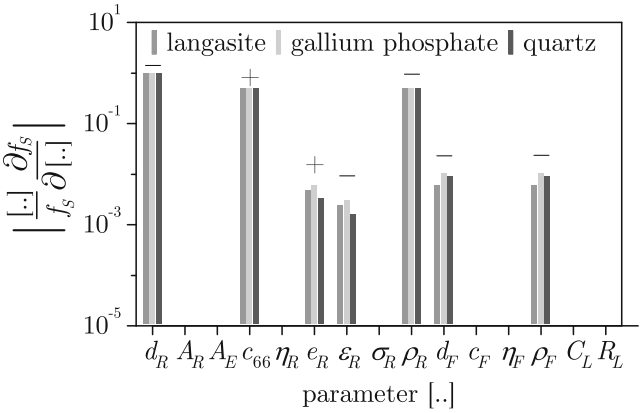

Fig. 11 Relative derivatives of the series resonance frequency for the parameters of the resonator device calculated for different materials at room temperature

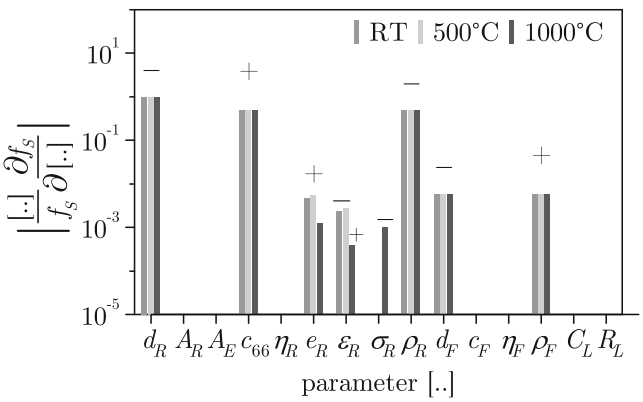

Fig. 12 Relative derivatives of the series resonance frequency for the parameters of the resonator device calculated for langasite at different temperatures

cause the strongest impact. Since the conductivity σ_R and the viscosity η_R are commonly thermally activated, they might be subject to changes by several orders of magnitude. In contrast, the parameters d_R, c_{66} and ρ_R are expected to show a relatively weak temperature dependence. The conclusion is that changes in σ_R potentially govern the resonance frequency even if its relative derivative κ_σ is smaller than that for d_R, c_{66} and ρ_R.

Further, the impact of the materials parameters on the resonator quality factor is of particular interest. Its derivatives $\partial Q/\partial [..]$ for the parameters [..] are calculated and multiplied by $[..]/Q$ to get $\nu_{[..]}$

$$\nu_{[..]} = \frac{[..]}{Q}\frac{\partial Q}{\partial [..]} = \frac{[..]}{f}\frac{\Delta f}{\Delta [..]}. \tag{20}$$

which allows to relate relative changes

$$\frac{\Delta Q}{Q} = \nu_{[..]}\frac{\Delta [..]}{[..]}. \tag{21}$$

Figure 13 shows the result of the calculation for different temperatures. In general, d_R, c_{66}, η_R, e_R and ρ_R dominate the behavior. The most remarkable result is the increasing impact of A_R, A_E, e_R, ε_R and σ_R with increasing temperatures.

The comparison of ν_η and ν_σ with the other dominant parameters shows differences smaller than one order of magnitude, only. The fact must be discussed in concert with the expected changes in the corresponding parameters. Again, d_R, c_{66}, e_R and ρ_R undergo relatively small changes in a wide temperature range. On the other hand, η_R and σ_R exhibit changes of some orders in magnitude. Therefore, the latter parameters are expected to affect Q predominantly. The result meets the expectations since η_R and σ_R are introduced to reflect losses.

In summary, d_R, c_{66}, ρ_R and σ_R are identified as the most relevant properties for stable, i.e. environmental independent, operation of resonators at its series resonance frequency at elevated temperatures. Consequently, the dependence of these parameters from the environmental conditions and the underlying atomic mechanisms must be studied in detail.

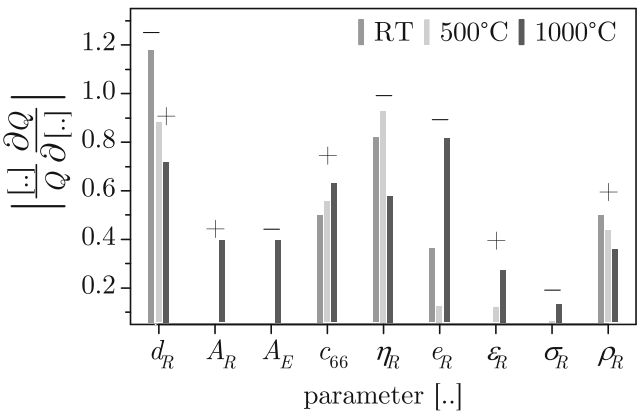

Fig. 13 Relative derivatives of the resonator quality factor for the parameters of the resonator device calculated for 5 MHz langasite resonator at different temperatures

3 Mass and charge transport

In order to take advantage of the high mass sensitivity of langasite resonators, environmental-independent operation must to be ensured. In other words, the stability of the most crucial properties must be evaluated as function of temperature and surrounding gas composition using a defect chemical approach.

The focus is put on stable resonance frequencies and low losses. According to [3], frequency fluctuations equivalent to noise of ±4 Hz can be defined as criterion to determine the range of stable operation of 5 MHz resonators. Extreme conditions such as

- High temperatures or low oxygen partial pressures and
- High concentrations of hydrogen containing species

potentially cause changes in the most relevant parameters c_{66}, ρ_R, σ_R and η_R and, thereby, frequency shifts larger than the limit mentioned above. The frequency shift might be explained by different scenarios including

- Formation of vacancies which primary impacts the density and potentially the strength of the interatomic bonds leading to modified elastic constants,
- Incorporation of hydrogenous species and
- Increase of the viscosity and conductivity due to the movement of ionic and electronic charge carriers. Thereby, moving ions are expected to show a stronger effect than electrons.

Initially, charge carriers and defects related to the presence of hydrogen are excluded by application of atmospheres containing residual amounts of hydrogen. In practice, the oxygen partial pressure (p_{O2}) is adjusted by CO/CO_2 gas mixtures. Under such conditions, the remaining hydrogen or hydrogenous species are found to impact the defect chemistry of langasite in a minor way.

Systematic measurements at reduced total pressure are not performed. However, short-term annealing runs

in vacuum do not result in obvious degradation of langasite.

3.1 Diffusive transport

First, the diffusivities of the relevant constituents and of potential dopants are presented. These results point to the most mobile charge carriers and enable to calculate the time constants of equilibration processes. Whenever possible, diffusion experiments and conductivity measurements are performed using langasite single crystals. However, the preparation of doped samples and the need to achieve reasonable equilibration times require, in some cases, the application of polycrystalline samples.

3.1.1 Oxygen diffusion

The oxygen self-diffusion in langasite is studied in the temperature range from 600 to 1000°C by oxygen isotope exchange experiments using $^{18}O_2$ enriched atmospheres and subsequent analysis of the ^{18}O depth profiles by secondary ion mass spectrometry (SIMS). Details about the experiments and the data evaluation are given in Appendix C. The correlation factor for the diffusion of the oxygen tracer is close to unity for a vacancy mechanism. Therefore, the tracer diffusion coefficient and the chemical diffusion coefficient are not distinguished.

Figure 14 shows the results for single crystalline (*sc*) and polycrystalline (*pc*) langasite in form of an Arrhenius plot. For the single crystals, the diffusion coefficients along the *y*-direction are given. The values for the *z*-direction are slightly larger (not shown). The plot indicates that oxygen diffusion is controlled by a single mechanism in the temperature range from 600 to about 1000°C, i.e. the activation energy E_A according to

$$D_O = D_0 e^{-E_A/k_B T} \tag{22}$$

is constant for the respective sample. Section 4 summarizes the values of E_A and of the temperature independent pre-exponential factor D_0.

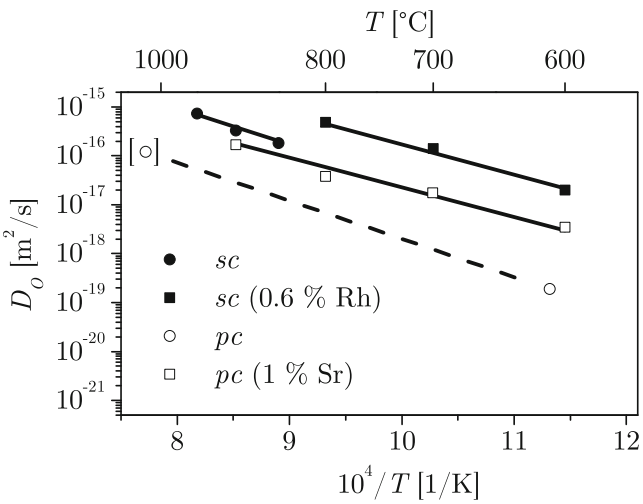

Fig. 14 Arrhenius plot of the oxygen diffusion coefficients. The curves denoted by *pc* and *sc* correspond to polycrystalline and single crystalline material, respectively. Considerable amounts of dopants are given in parenthesis

Small differences in magnitude and activation energy of the oxygen diffusion coefficients are observed for nominally undoped and 0.6% Rh containing langasite single crystals. According to Section 4, rhodium impurities could be neutral or act as donor. In the latter case, the electron concentration is expected to be increased thereby suppressing the oxygen vacancy concentration and oxygen diffusion. However, the experimental findings point to the inverse case leading to the conclusion that rhodium is neutral. Therefore, the differences observed in Fig. 14 may be related to other background impurities or intrinsic non-stoichiometries of the crystals.

The calculated diffusion coefficients of polycrystalline langasite are lower than that of the single crystals. This discrepancy is potentially caused by the large error in estimation of diffusion coefficients in polycrystalline samples using the technique described in Appendix C. The approach requires high quality data. For the polycrystalline specimens which show a relatively low density, tracer diffuses rapidly through the pores by gas phase diffusion, thereby implying a very high boundary diffusion which effectively masks bulk contributions. Therefore, only two (less reliable) data points could be extracted for nominally undoped polycrystals. Niobium doped langasite shows even higher porosities which prevents any reasonable data evaluation.

Sr doped samples could be evaluated. The addition of the acceptor, in this specific example 1% Sr, markedly increases the oxygen diffusion. The observation supports the defect model (see Section 4) since acceptor doped langasite is expected to show an even higher ionic conductivity due to the increased oxygen vacancy concentration.

3.1.2 Hydrogen diffusion

Hydrogen or hydrogenous species are generally suspected to contribute substantially to the mass and

charge transport [73]. Therefore, their chemical diffusion is investigated. The annealing of the samples in 6% H_2/Ar results in very flat depth profiles even if the annealing time is in the order of minutes, only. Within the depth accessible by SIMS, the concentration does not show significant changes. Further, the penetration of hydrogenous species from both surfaces of the sample overlaps potentially. As a consequence, the data cannot be evaluated using Fick's second law. Alternatively, the time dependent hydrogen content inside the samples can be used to estimate the diffusion coefficient. The approach bases on the description of the total content of the diffusing species as function of its diffusion coefficient and annealing time. The approach and its reduction to practice using the actual samples are described in [74] and [70], respectively. Thereby, the OH-content is determined by Fourier Transform InfraRed (FT-IR) spectroscopy using the absorption peak at 3,400 cm^{-1}. The 0.5 mm thick samples are annealed in 6% H_2/Ar at 600°C for different periods of time and subsequently analyzed. The resulting normalized OH-content is shown in Fig. 15. For reference, the OH-content is determined by SIMS. However, the data are not reliable since the system was operated close to the resolution limits. The fact causes the large scattering of these data points in Fig. 15.

The diffusion coefficient found at 600°C is 1.12×10^{-11} m^2/s. The value is orders of magnitude higher than that of oxygen. Therefore, a dominant role of hydrogen must be encountered.

3.1.3 Cation diffusion

Gallium is known to contribute substantially to the ionic conduction in systems such as $NdAlO_3$-$NdGaO_3$ [75] and (La,Sr)(Ga,Ni)O_3 [76] and, therefore, suspected to play a significant role in langasite. Consequently, the diffusivity of gallium must be determined to evaluate its contribution to the ionic conductivity. Contrary, silicon is, in general, covalently bound and lanthanum is large. Therefore, it is unlikely that both ions migrate easily within langasite.

The gallium self-diffusivity is determined in single crystalline langasite by implantation of the stable isotope ^{71}Ga, subsequent annealing and depth profile analysis. Details about the data evaluation are given in Appendix C.

Figure 16 shows the resulting diffusion coefficients. The activation energy of 3.13 eV is significantly higher than that of oxygen diffusion. Moreover, the gallium diffusion is orders of magnitude less than the oxygen diffusion. Therefore, gallium does not contribute significantly to conduction and can be dismissed from that standpoint. The related surface exchange coefficient is discussed in Section 3.2.

Further, the chemical diffusion of potential dopants (see Section 4) is investigated. Their diffusivity is of interest since local doping is an option to form highly conductive areas or to modify the rate of chemical etch processes. These diffusion coefficients are determined using thin films as source for the diffusing species. The diffusion coefficients of strontium, praseodymium and niobium are fairly small as shown in Fig. 16. Remarkably, strontium and praseodymium exhibit virtually the same diffusivity which is consistent with their similar ionic radii and the occupation of the same site in the langasite lattice.

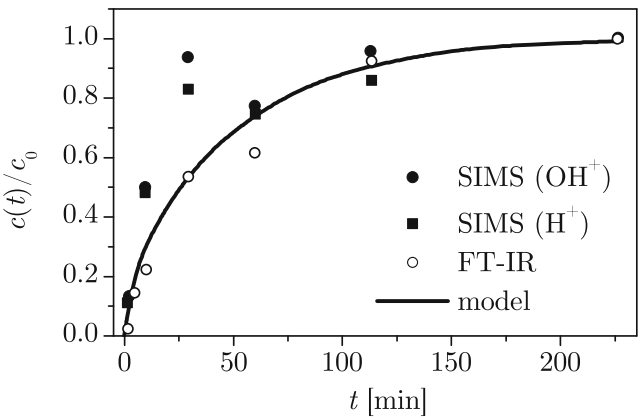

Fig. 15 Normalized OH-content of single crystalline langasite as function of time during annealing in 6% H_2/Ar at 600°C [70]

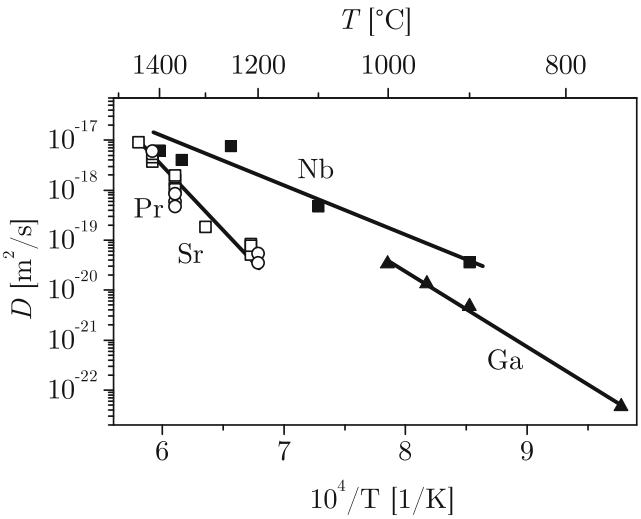

Fig. 16 Arrhenius plot of the diffusion coefficients of gallium and potential dopants along the *y*-direction in langasite single crystals

The characteristic diffusion depth along the y-axis y_D can be estimated from the diffusion coefficient and the annealing time t according to

$$y_D = 2\sqrt{Dt}. \tag{23}$$

At 1400°C, where the diffusion coefficients of strontium, praseodymium and niobium are quite similar, a diffusion depth of 5 µm requires annealing periods of several days. Consequently, the preparation of locally doped langasite samples by thermal diffusion might be time consuming and prevent the application of the method. Alternatives are the epitaxial deposition of doped langasite layers [77] or the field enhanced diffusion. Contrary, once the doping is performed, operation temperatures of 900°C virtually do not change the extent of the doped region. For example, y_D increases for strontium or praseodymium from 3.0 to 3.1 µm within 4,000 years.

3.2 Gallium loss

So far, reversible changes in materials properties of langasite are reported. However, unfavorable conditions such as extremely high temperatures and low oxygen partial pressures are suspected to reduce the material or to result in gallium loss. Reduction of langasite leading to irreversible modifications is not observed for the experimental conditions described in the previous sections. In contrast, gallium loss occurs at 900°C at or below $p_{O2} = 10^{-17}$ bar in CO/CO_2 atmospheres. Figure 17 presents SIMS depth profiles for the cations gallium, lanthanum and silicon. Thereby, the acquired data are normalized to the background concentration of given elements within langasite. The curves denoted by (1) are determined after annealing of single crystalline langasite for 24 h at the conditions mentioned above. A significant decrease in gallium concentration is observed in a surface region of about 1.5 µm. Obviously, the gallium concentration forms a plateau near the surface and does not fall below about 5% which corresponds to the ratio of gallium to silicon of about unity at the surface (see Table 3). The observations imply that only sixfold coordinated gallium at the B-sites remains in the sample. The occurrence of the B-site is 4.3%. In other words, the fourfold coordinated gallium is obviously removed from the lattice. Unfortunately, analysis by X-Ray Diffractometry (XRD) do not deliver conclusive information about the phase at the surface.

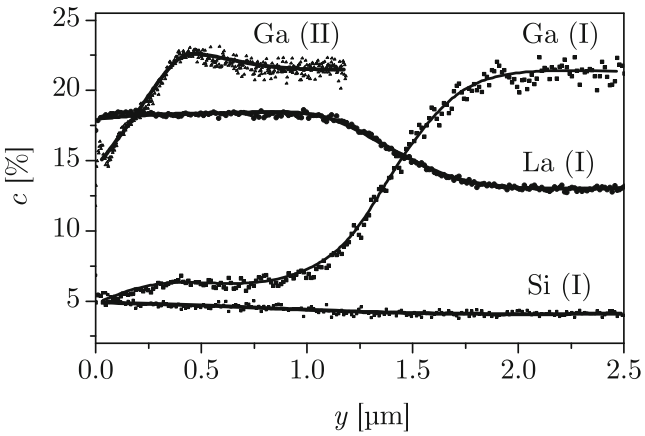

Fig. 17 Concentration depth profiles for the gallium, lanthanum and silicon after different annealing steps (see text) determined by SIMS

A second annealing of the same sample in air (900°C, 24 h) results in an increase in gallium concentration at the surface. In particular, the formerly gallium-depleted area is almost filled by outward diffusion of gallium. The curve denoted by Ga(II) in Fig. 17 visualizes the situation. Consequently, the gallium loss at the surface must be largely suppressed at high p_{O2}. The observation goes along with that for Ga_2O_3 reported in [78] where the partial pressure of the volatile gallium suboxide Ga_2O decreases with increasing p_{O2}.

The annealing leads to a decrease of the total gallium content. An uniform decrease is expected for low evaporation rates where the chemical diffusion maintains a nearly constant gallium concentration. However, small changes as estimated for the actual sample cannot be detected due to the limited resolution of the analytical tools. Therefore, the gallium loss is calculated using the surface exchange coefficient K_{Ga} which is a secondary result of the diffusion measurements. It must be noted that the diffusion annealing is performed in air. In order to back up the approach, the surface exchange coefficients are calculated from the difference in the integrals of the gallium concentration profiles determined by SIMS before and after annealing. The difference provides information about the gallium loss for a given annealing time. The surface exchange coefficients determined by both approaches are presented in Fig. 18.

Table 3 Surface concentration after annealing (900°C, $p_{O2} = 10^{-17}$ bar, 24 h) determined by Wavelength Dispersive X-ray spectroscopy (WDX)

Concentration c [%]				c_{Ga}/c_{Si}
La	Ga	Si	O	
26.01	9.44	8.94	55.62	1.06

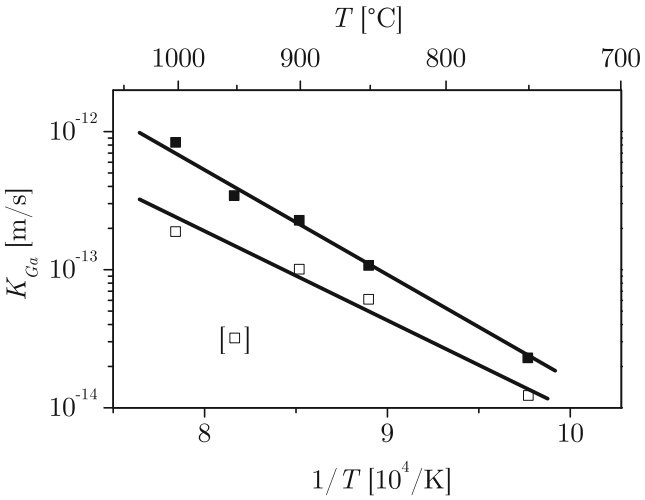

Fig. 18 Gallium surface exchange coefficients for single crystalline langasite at ambient oxygen partial pressure

The difference of the results is fairly small and can be explained by the errors of measurement.

If the surface exchange determines the gallium loss solely, samples held at 750 and 900°C in air lose one monolayer of gallium (6.6×10^{14} atoms/cm^2) within 10 and 1 h, respectively. Therefore, the gallium loss is negligible at 750°C and high p_{O2}. Even at 900°C a surface layer of 1.5 μm would be depleted within 160 days, only. The estimation ignores the chemical diffusion of gallium within langasite. The situation changes in reducing CO/CO_2 atmospheres as demonstrated above. At 900°C, the gallium loss is increased by a factor of 160.

An essential consequence for the operation of langasite-related compounds under extreme conditions, i.e. high temperatures and reducing CO/CO_2 atmospheres, is to use compositions which contain less gallium. A possibly suited gallium-free material is $La_3SbZn_3Ge_2O_{14}$ [79].

3.3 Equilibration times

Single crystalline langasite samples exhibit time dependent materials properties as long as they are not heated to high temperatures. To quantify this fact, the minimum temperature for achieving equilibrium conditions of the oxygen stoichiometry can be estimated by solving Eq. 23 for $D(T)$. Taking the thickness of a 5 MHz langasite resonator $y_D = d_R/2 \approx 135$ μm and equilibration times in the order of several hours as example, temperatures of at least 1050°C are required. For the calculation an extrapolated oxygen diffusion coefficient according to Eq. 22 is used. As a consequence, the single crystalline samples presented in this work are pre-annealed for at least 24 h at or above 1050°C. Exceptions are indicated.

Contrary, below about 1000°C equilibrium conditions for oxygen stoichiometry cannot be expected within reasonable periods of time for the given dimensions of the langasite crystals. The fact is particular unfavorable for p_{O2} dependent conductivity measurements. Dimensions in the order of few micrometers would be required. Alternatively, polycrystalline langasite samples obviously providing fast transport paths can be used for such measurements. These insights motivate the fundamental decision to evaluate the defect chemistry of langasite based on polycrystalline samples.

However, polycrystalline samples do not enable the investigation of piezoelectric properties. Single crystals must be applied which results to some extend in time dependent materials properties. Pre-annealing does not solve the problem of non-equilibration at medium and low temperatures. However, relatively strong fluctuations of the materials properties occurring during the first annealing are not observed anymore. Therefore, the use of pre-annealed single crystalline samples is the only feasible option to determine the piezoelectric properties. In order to recognize potential errors, special attention must be drawn on time dependent fluctuations of the properties. At this point it should be noted that long term experiments at 600°C do not indicate fluctuations of the piezoelectric properties.

The hydrogen diffusion coefficient of 1.12×10^{-11} m^2/s at 600°C enables to estimate the time to saturate langasite with hydrogen or hydrogenous species at that temperature. Taking again the thickness of a 5 MHz langasite resonator $y_D = d_R/2 \approx 135$ μm, the calculation according to Eq. 23 results in 108 min. The saturation time at higher temperatures is even shorter. Consequently, time independent conditions with respect to the hydrogen content of the samples could be realized easily during the experiments in hydrogenous atmospheres.

3.4 Electrical conductivity

The electrical conductivity of langasite is measured in the temperature range from 400 to 1050°C. In the first part of this section, the conductivity data of polycrystalline langasite presented in [80–82] are summarized. These results are compared with that of single crystalline langasite in the second part.

Assuming diffusive transport which is appropriate for either ionic or electron hopping, the activation energy of the process is preferably derived from the temperature dependence of the conductivity-temperature

product (see Section 3.5). In case of e.g. electron migration, the activation energy is directly related to the conductivity and extracted from its temperature dependence. Since the dominant process is, a priori, not clear the plots show in general the conductivity. Nevertheless, the activation energy is determined from the conductivity-temperature product whenever applies.

3.4.1 Hydrogen free atmospheres

Nominally undoped polycrystalline langasite exhibits p_{O2} independent electrical conductivity at medium and high p_{O2} as visualized in Fig. 19. Here, the bulk conductivity σ_B is shown which reflects the conductivity of the grains. The value can be compared with the conductivity σ_R of the langasite single crystals. Accompanying concentration cell and thermoelectric power measurements confirmed the dominance of ionic conduction [80–82].

With decreasing p_{O2}, the conductivity increases indicating predominant electronic conduction. The $-1/4$ slope in the log – log plot becomes obvious by subtracting the ionic part from the total conductivity (not shown).

Donor doped polycrystalline langasite shows a p_{O2} independent conductivity at medium and high p_{O2}, too. However, the accompanying concentration cell and thermoelectric power measurements points to predominant electronic conduction. With decreasing p_{O2}, an even enhanced electronic conduction with a $-1/6$ slope is found as seen in Fig. 20.

The conductivity of acceptor doped langasite is shown in Fig. 21. In contrast to the nominally undoped and the donor doped material, the p_{O2} independent conductivity occurs at low and medium p_{O2}. Here, ionic conduction dominates. Further, the plot indicates p-type electronic conduction at high p_{O2}. A slope of 1/4 becomes obvious by subtracting the ionic part from the total conductivity (not shown).

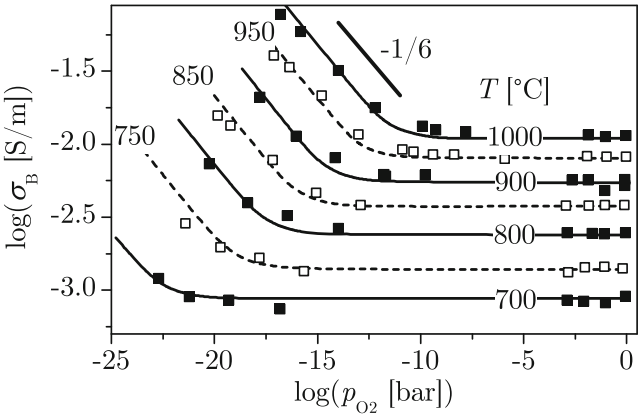

Fig. 20 Oxygen partial pressure dependent conductivity of donor doped polycrystalline langasite (5% Nb) taken from [83]

The comparison of Figs. 19–21 shows almost identical conductivities of nominally undoped and donor doped polycrystalline langasite in the p_{O2} independent range, i.e. at medium p_{O2}. The equality is seen as coincidental phenomenon since the predominant charge carrier type differs. At low p_{O2}, donor doping leads to enhanced electronic conduction.

Acceptor doping increases the conductivity by about one order of magnitude at medium p_{O2} as illustrated in Fig. 22. The fact goes along with the increase in oxygen diffusion by about one order of magnitude as seen in Fig. 14 for polycrystalline langasite and confirms the dominance of ionic conduction. Further, the result corresponds to the conductivity prediction presented

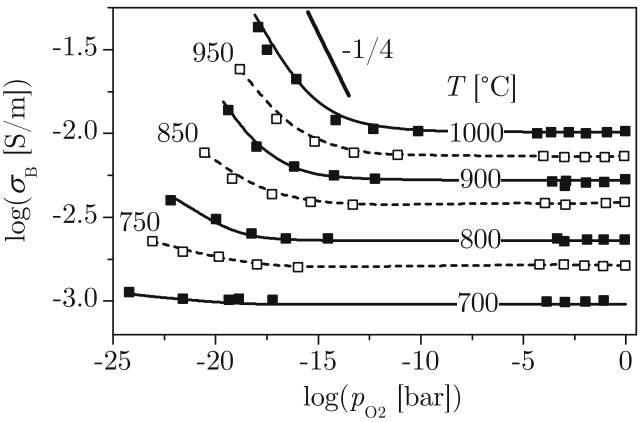

Fig. 19 Oxygen partial pressure dependent conductivity of nominally undoped polycrystalline langasite taken from [83]

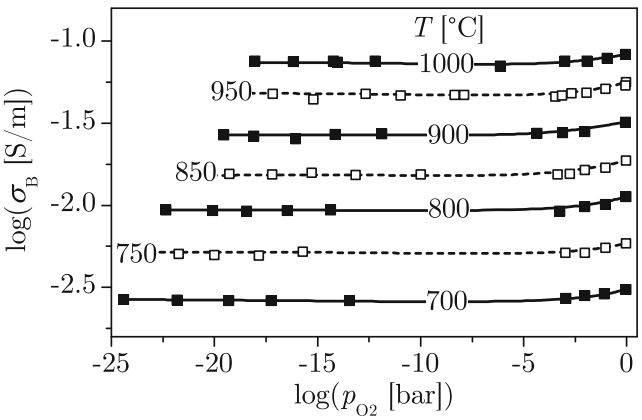

Fig. 21 Oxygen partial pressure dependent conductivity of acceptor doped polycrystalline langasite (1% Sr) taken from [83]

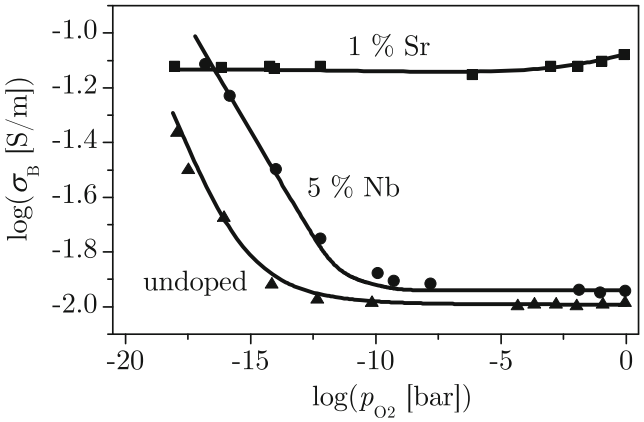

Fig. 22 Oxygen partial pressure dependent conductivity at 1000°C for nominally undoped, acceptor (1% Sr) and donor (5% Nb) doped polycrystalline langasite

in Section 4 (see Fig. 32) for an increase in net donor concentration from $[A'_C] - [D^{\bullet}_C] \gtrsim 0$ to 1% Sr. These statements remain largely true for high p_{O2}. Even at $p_{O2} = 0.2$ bar, the *p*-type electronic conduction causes an increase in conductivity of about 7%, only. Fully *p*-type conduction is expected for higher doping levels and/or higher p_{O2}.

In the p_{O2} independent range, the temperature dependence of the conductivity-temperature product enables to extract the activation energy of the ionic transport in nominally undoped and acceptor doped langasite. The property is visualized in Fig. 23. The activation energy of the electron transport in donor doped langasite is found to be 0.91 eV which is interpreted as sum of donor ionization and electron migration energies [80–82]. The activation energy for strontium doped langasite is significantly larger which goes along with the activation energy of the oxygen diffusion. Numerical values for the activation energies are summarized in Table 4.

Table 4 Activation energy of the conductivity in langasite in the p_{O2} independent range

Langasite	Property	E_A [eV]	Temperature range [°C]
sc	σ_B	0.82	400–700
	$\sigma_B T$	1.15	700–1050
sc (0.5% Sr)	$\sigma_B T$	0.98	400–550
	$\sigma_B T$	1.39	550–950
sc (0.5% Nb)	σ_B	0.91	400–550
	σ_B	1.29	550–950
pc	$\sigma_B T$	0.91	750–1000
pc (1% Sr)	$\sigma_B T$	1.27	700–1000
pc (5% Nb)	σ_B	0.91	700–1000

Further, the magnitude of the conductivity of nominally undoped single crystalline and polycrystalline langasite is compared. Figure 24 shows orientation dependent conductivities for the single crystalline material which differ by about one order of magnitude. The effective conductivity of polycrystalline materials results from the statistical orientation of the grains. The limits are given by [84]

$$\sqrt[3]{\sigma_x^2 \sigma_z} \leq \sigma_B \leq \frac{1}{3}(2\sigma_x + \sigma_z) \tag{24}$$

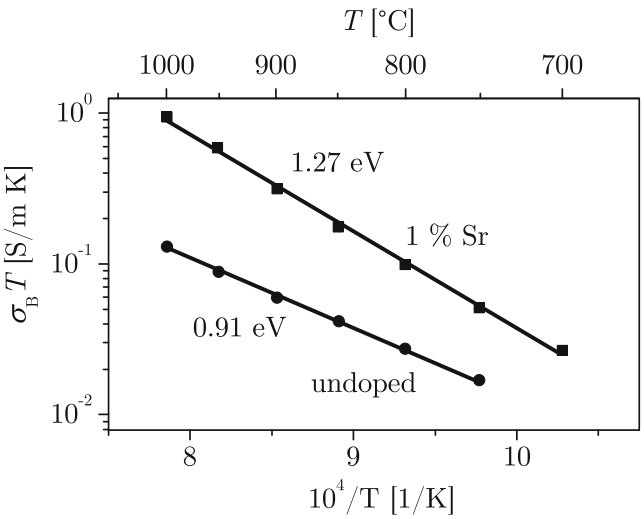

Fig. 23 Arrhenius plot of the conductivity-temperature product for nominally undoped and acceptor (1% Sr) doped polycrystalline langasite in the p_{O2} independent range and indication of the respective activation energy

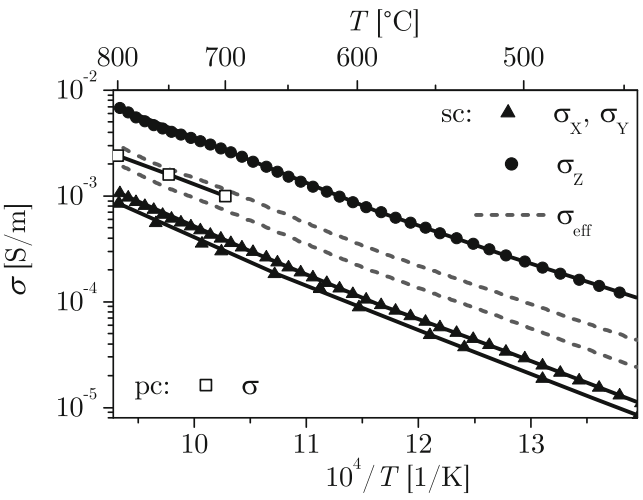

Fig. 24 Electrical conductivity of langasite single crystals ($\sigma_x = \sigma_y$ and σ_z) and of polycrystalline langasite (σ_B) at $p_{O2} = 0.2$ bar. The predicted range of the effective conductivity of polycrystalline langasite (σ_{eff}) is indicated

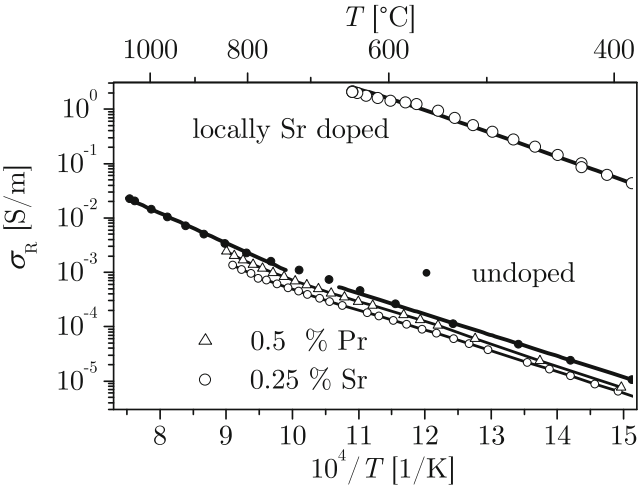

Fig. 25 Conductivity of nominally undoped, 0.25% Sr and 0.5% Pr doped single crystalline langasite as well as conductivity of a strontium doped layer at $p_{O2} = 0.2$ bar

and indicated in Fig. 24. It is clearly obvious that the measured conductivity of polycrystalline langasite falls within these limits. Consequently, the differently prepared materials satisfy this condition necessary to be comparable.

The electrical conductivity of undoped langasite as presented in Fig. 25 shows a clear change in activation energy at about 700°C. The observation is highly remarkable since it indicates a change in the dominant conduction mechanism. The suspicion is supported by the following arguments:

- The electronic conduction dominates below about 700°C. The comparison with the ionic conductivity as done in Section 3.5 supports this statement. Further, the activation energy of the total conductivity of *n*-type polycrystalline (donor doped) and single crystalline langasite is close and, in particular, lower than that of the oxygen diffusion. The facts become obvious by the values in Tables 4 and 5.
- The ionic conduction takes over the total conductivity above about 700°C. The activation energy of the oxygen diffusion is found to be higher than that of the electronic conduction which leads to an increased impact of the former with increasing temperature. Further, similar activation energies of the total conductivity and the oxygen diffusion are observed in this temperature range.
- The previous arguments are strongly supported by a direct demonstration of the change in dominating charge carrier type by measurements of the ionic transfer number [85]. The effect is shown at 720°C for the langasite-related compound langatate ($La_3Ta_{0.5}Ga_{5.5}O_{14}$).

These arguments turn the above mentioned suspicion in a fact, i.e. the conduction in the nominally undoped langasite prepared by the Czochralski technique is dominated by electronic carriers below 700°C and turns in predominant ionic conduction above that temperature. In other words, the material behaves like net donor and acceptor doped langasite below and above 700°C, respectively. Since undoped langasite is always operated close to this transition, the presumably strong effect of moving oxygen ions on damping must be expected even at low temperatures.

Finally, the impact of dopants is evaluated. Figure 25 compares the conductivity of nominally undoped, 0.25% Sr and 0.5% Pr doped langasite single crystals. It becomes obvious that light doping changes the conductivity in a minor way.

In order to determine the impact of heavy strontium doping on the conductivity locally doped areas are prepared by inward diffusion of strontium using SrO as source. The langasite samples evaluated here exhibit a strontium concentration of up to 6×10^{21} cm^{-3} in an effectively 2.7 μm thick surface layer. About 60% of lanthanum are expected to be replaced by strontium which is in agreement with the option to replace lanthanum largely [33]. The change in conductivity of the locally doped area is found to be three to four orders in magnitude as visualized in Fig. 25.

Further, a second homogenously doped langasite crystal containing 0.5% Sr is investigated. The material shows a considerable decrease in conductivity as visualized in Fig. 26.

Doping with 0.5% Nb is performed in order to explore the effect of donors. Niobium doped langasite

Table 5 Activation energy and pre-exponential factor of diffusion in langasite

Langasite	Species	E_A [eV]	D_0 [m^2/s]	Temperature range [°C]
sc	^{18}O	1.25	7.6×10^{-6}	750–950
sc (0.6% Rh)	^{18}O	1.22	2.5×10^{-6}	600–800
pc (1% Sr)	^{18}O	1.20	2.6×10^{-7}	600–900
sc	^{71}Ga	3.33	9.1×10^{-8}	750–1000
sc	Sr, Pr	4.50	1.1×10^{-4}	1200–1450
sc	Nb	1.83	2.8×10^{-8}	900–1400

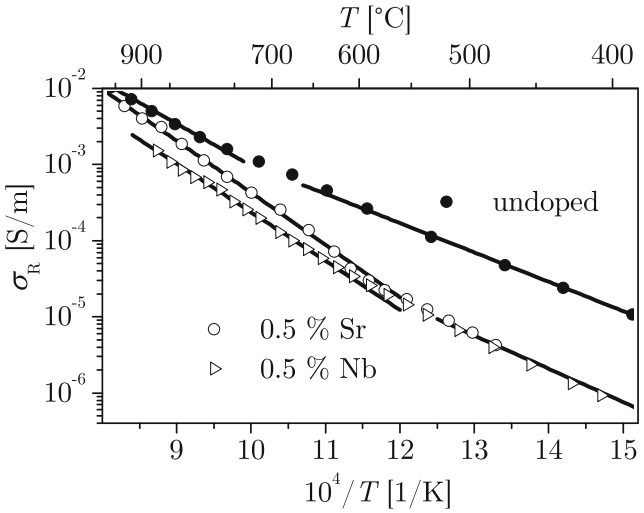

Fig. 26 Conductivity of nominally undoped, 0.5% Sr and 0.5% Nb doped single crystalline langasite at $p_{O2} = 0.2$ bar

shows a lower conductivity than undoped single crystals. Obviously, the material is effectively compensated. Remarkably, the activation energy of the conduction is lower than that of strontium doped langasite.

3.4.2 Hydrogen containing atmospheres

The p_{O2}-dependence of the conductivity in hydrogenous atmospheres differs from that in nominally hydrogen free atmospheres. The fact is visualized in Fig. 27 where the conductivity decreases with decreasing p_{O2}. The difference in conductivity by about half an order of magnitude at 800°C goes along with the fact that *y*-cut single crystalline and polycrystalline langasite are compared. Consequently, the origin of the decreasing conductivity with decreasing p_{O2} remains to

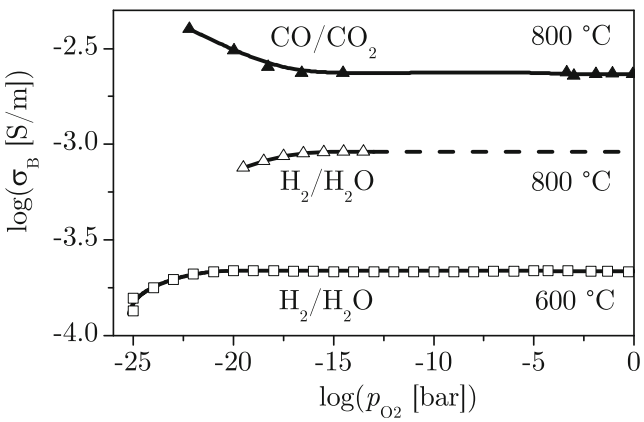

Fig. 27 Oxygen partial pressure dependent conductivity of langasite in hydrogenous and nominally hydrogen free atmospheres

be explained. The further presentation of the results is preferably done using the p_{H2O}-dependence of the conductivity since the corresponding equations for *z*-cut and *y*-cut langasite introduced in Section 4 show distinct relations.

The experimental results presented in Fig. 28 indicate a 1/2 dependence of the conductivity along the *z*-axis at 800°C in the $\log(\sigma_B) - \log(p_{O2})$ plot. The same applies at 600°C (not shown). For the actual resonators, the properties along the *y*-axis are of particular interest. Here, Fig. 28 shows a $1/2 - 0.07$ and $1/2 - 0.3$ dependence at 600 and 800°C, respectively.

3.5 Ionic conductivity

The cation diffusion data indicate that oxygen ions are the only ionic charge carriers which might contribute significantly to the total electrical conductivity. Assuming an oxygen transport mechanism via oxygen vacancies, the contribution of oxygen transport

$$\sigma_O = q_V [V_O^{\bullet\bullet}] \mu_V \tag{25}$$

to the total conductivity may be calculated based on the measured oxygen tracer diffusion. The oxygen vacancy concentration $[V_O^{\bullet\bullet}]$ and mobility μ_V can be eliminated using the Einstein relation [86, 87]

$$\frac{k_B T}{q_V} \mu_V = D_V \tag{26}$$

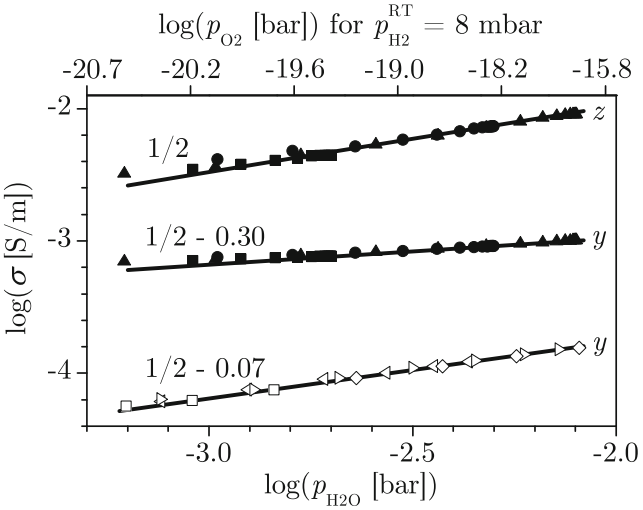

Fig. 28 Water vapor pressure dependent conductivity of single crystalline langasite at 800 (*solid symbols*) and 600°C (*open symbols*). The shape of the symbols corresponds to different levels of hydrogen provided to the reaction chamber (p_{H2}^{RT} range: 2–18 mbar) [62, 70]

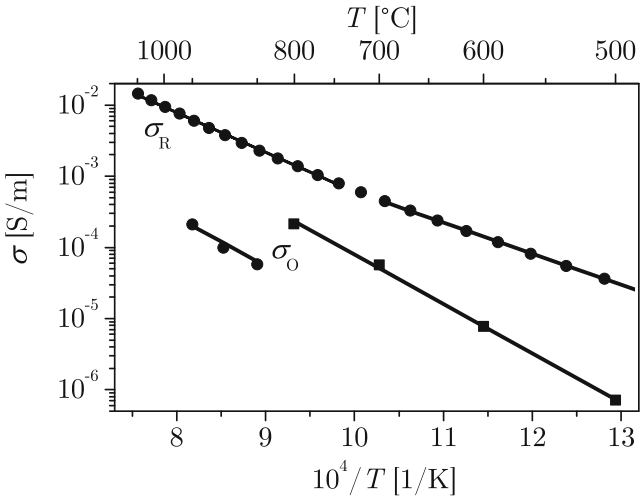

Fig. 29 Total bulk and oxygen ion conductivities in langasite as a function of reciprocal temperatures

and

$$D_O[O_O] = D_V[V_O^{\bullet\bullet}] \tag{27}$$

where k_B, T, $[O_O]$, $q_V = 2q$ and D_V are the Boltzmann constant, the absolute temperature, the oxygen concentration, the charge of the mobile species and vacancy diffusion coefficient, respectively. The calculation yields

$$\sigma_O = \frac{(2q)^2}{k_B T}\left[O_O\right] D_O. \tag{28}$$

At 800°C, σ_O results in 2.1×10^{-4} S/m. The value corresponds to about 15% of the total conductivity as it can be seen in Fig. 29. At 600°C an ionic contribution of 5% is found.

4 Defect model

Langasite can be doped by a variety of cations. The sites where they substitute into are known [33, 88–90]. Based on the ionic radii and the coordination numbers strontium or praseodymium dopants occupy La^{3+} sites (A site). Under these circumstances, strontium acts as acceptor whereas praseodymium is a neutral substituent or a donor. Niobium replaces Ga^{3+} thereby acting as donor. Rhodium impurities originating from the growth process in Pt/Rh crucibles are expected to occupy Ga^{3+} sites and act as donor for Rh^{4+} or Rh^{5+} valence states. In case of the absence of acceptors, the charge compensation would be fulfilled by electrons. Another option is the appearance of Rh^{3+} which does not change the charge with respect to the lattice.

Table 6 Sites, potential dopants, their oxygen coordination and ionic radii [44]

Site	Dopant	Oxygen coordination	Ionic radii [10^{-10} m]	Effect
A	Sr^{2+}	8	1.26	Acceptor
A	Pr^{3+}	8	1.13	Neutral
A	Pr^{4+}	8	0.96	Donor
B	Nb^{4+}	6	0.68	Donor
B	Nb^{5+}	6	0.64	Donor
C,D	Nb^{5+}	4	0.48	Donor
B	Rh^{3+}	6	0.67	Neutral
B	Rh^{4+}	6	0.60	Donor
B	Rh^{5+}	6	0.55	Donor

Table 6 lists potential dopants, their coordination numbers and ionic radii. These substitutions are in accordance with the subsequently presented defect model which reflects the effect of these dopants consistently.

4.1 Nominally hydrogen-free environments

The defect model presented in the following summarizes parts of the detailed description given in [80–82]. Key defect reactions are selected whereby the formation of oxygen vacancies $V_O^{\bullet\bullet}$ (Kröger–Vink notation [91]) at low p_{O2} is the most relevant feature with respect to mass changes of the resonator material leading potentially to frequency shifts of resonator devices. These reactions and their mass action laws are the

- Reduction,

$$O_O^{\times} \leftrightarrow V_O^{\bullet\bullet} + 2e' + 1/2\ O_2 \tag{29}$$

$$k_R = \left[V_O^{\bullet\bullet}\right] n^2 p_{O2}^{1/2} \tag{30}$$

- Oxidation,

$$1/2\ O_2 + V_O^{\bullet\bullet} \leftrightarrow O_O^{\times} + 2h^{\bullet} \tag{31}$$

$$k_O = p^2 \left[V_O^{\bullet\bullet}\right]^{-1}\ p_{O2}^{-1/2} \tag{32}$$

- Generation of electrons and holes,

$$null \leftrightarrow h^{\bullet} + e' \tag{33}$$

$$k_E = n\,p \tag{34}$$

- Schottky reaction and

$$null \leftrightarrow 14V_O^{\bullet\bullet} + 3V_{La}''' + 5V_{Ga}''' + V_{Si}'''' \tag{35}$$

$$k_S = \left[V_O^{\bullet\bullet}\right]^{14} + \left[V_{La}'''\right]^3 + \left[V_{Ga}'''\right]^5 + \left[V_{Si}''''\right] \tag{36}$$

- Anion Frenkel reaction.

$$O_O^{\times} \leftrightarrow V_O^{\bullet\bullet} + O_i'' \tag{37}$$

$$k_F = \left[V_O^{\bullet\bullet}\right]\left[O_i''\right]. \tag{38}$$

Further, for dopants additional reactions and mass action laws for the

- Ionization of acceptors and

$$A \leftrightarrow A_C' + h^{\bullet} \tag{39}$$

$$k_A = \left[A_C'\right] p \tag{40}$$

- Ionization of donors

$$D \leftrightarrow D_C^{\bullet} + e' \tag{41}$$

$$k_D = \left[D_C^{\bullet}\right] n \tag{42}$$

apply. The subscript C represents cation sites. Manifold charges with respect to the lattice do not have to be introduced since the model describes the experimental findings consistently.

Finally, the general neutrality equation for electrical charges in the crystals

$$2\left[V_O^{\bullet\bullet}\right] + p + \left[D_C^{\bullet}\right] = 2\left[O_i''\right] + n + \left[A_C'\right] \tag{43}$$

must be fulfilled.

The solution of the above set of equations provides the relation between temperature, oxygen partial pressure, dopant level and concentrations c_l of charge carriers indexed by l. The latter enable the calculation of the partial conductivities σ_l provided that their charges q_l and mobilities μ_l are known. Thus, the experimentally accessible total conductivity σ_B follows from[4]

$$\sigma_B = \sum_l \sigma_l = \sum_l q_l\, \mu_l\, c_l. \tag{44}$$

The complexity of the set of equations can be reduced by applying the Brouwer approximation [92] where a dominating defect relation is regarded in restricted ranges of temperature and p_{O2}. Accordingly, the neutrality equation includes a single dominating type of positive and negative charge carrier, only.

Even nominally undoped langasite is expected to exhibit some intrinsic non-stoichiometry and, therefore, to behave like net donor or acceptor doped material. Under such circumstances, typical defect regions and their neutrality equations are the

- Reduction,

$$n \approx 2\left[V_O^{\bullet\bullet}\right] \tag{45}$$

- Ionic compensation,

$$2\left[V_O^{\bullet\bullet}\right] \approx \left[A_C'\right] \quad \text{for} \quad \left[A_C'\right] > \left[D_C^{\bullet}\right] \tag{46}$$

$$2\left[O_i''\right] \approx \left[D_C^{\bullet}\right] \quad \text{for} \quad \left[D_C^{\bullet}\right] > \left[A_C'\right] \tag{47}$$

- Electronic Compensation and

$$p \approx \left[A_C'\right] \quad \text{for} \quad \left[A_C'\right] > \left[D_C^{\bullet}\right] \tag{48}$$

$$n \approx \left[D_C^{\bullet}\right] \quad \text{for} \quad \left[D_C^{\bullet}\right] > \left[A_C'\right] \tag{49}$$

- Oxidation.

$$p \approx 2\left[O_i''\right] \tag{50}$$

Among other conclusions, these equations enable the calculation of the p_{O2}-dependence of the charge carrier concentrations. Criteria to identify the partial conductivity σ_l which dominates the total conductivity σ_B are the concentration and the mobility of the different charge carriers. The concentrations can be taken from the defect model. The mobilities of the ions follow from the diffusivities presented in Section 3.1. It turns out that oxygen vacancies are the only ionic carriers which contribute substantially to the conductivity. Of course, electrons (and holes) must be considered since they are in general significantly more mobile than ions.

Taking net acceptor doped material as example, the concentration of oxygen vacancies is fixed according to Eq. 46 at sufficiently high p_{O2}. Further, electrons are suppressed which results in predominant ionic conduction carried by oxygen vacancies. Consequently, the dominating charge transport is p_{O2} independent

$$\sigma_B \sim [V_O^{\bullet\bullet}] \neq f(p_{O2}). \tag{51}$$

With decreasing p_{O2} electrons are generated and take over the conductivity σ_B even if their concentration is lower than that of oxygen vacancies. The former are expected to be more mobile than oxygen vacancies. Under such circumstances, the p_{O2}-dependence of the electron concentration and, thereby, of the conductivity follow from Eqs. 30 and 46

$$\sigma_B \sim n \sim p_{O2}^{-1/4}. \tag{52}$$

At very low p_{O2} the reduction reaction controls the formation of electrons and oxygen vacancies. The combination of Eqs. 30 and 45 results in the p_{O2}-dependence

$$\sigma_B \sim n \sim p_{O2}^{-1/6}. \tag{53}$$

The slope of the p_{O2}-dependence of the electron concentration in the subsequently presented log-log plots is $\Delta \log n / \Delta \log p_{O2} = -1/6$.

[4] The property σ_B reflects the bulk conductivity of polycrystalline or single crystalline langasite. In the latter case σ_B equals σ_R.

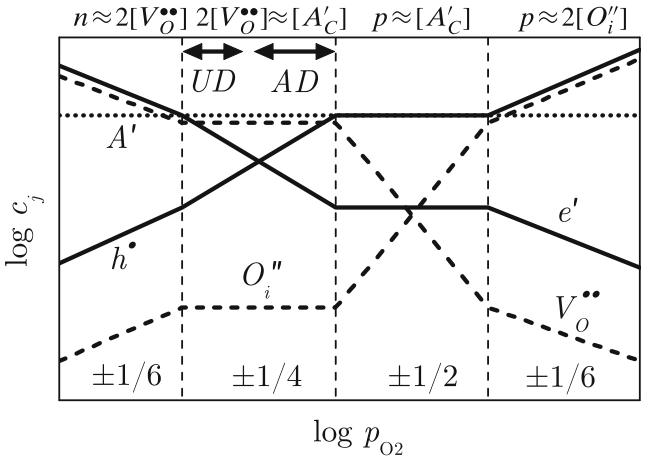

Fig. 30 Kröger–Vink diagram for net acceptor doped langasite and ranges of operation for nominally undoped (*UD*) and acceptor doped (*AD*) langasite taken from [83]

Calculations for the complete set of equations are presented in [80–82]. In the following these results are summarized by the Kröger-Vink diagrams for net acceptor and donor doped langasite and given in Figs. 30 and 31, respectively. The defect regions mentioned above are separated by vertical dashed lines and denoted by the dominating neutrality relation above the diagrams. Further, the modulus of the slope of the curves is indicated in the bottom part of the figures. The appropriate sign and vanishing slopes become obvious from the curves themselves. The example concerning acceptor doped langasite from above corresponds to the left hand regions in Fig. 30.

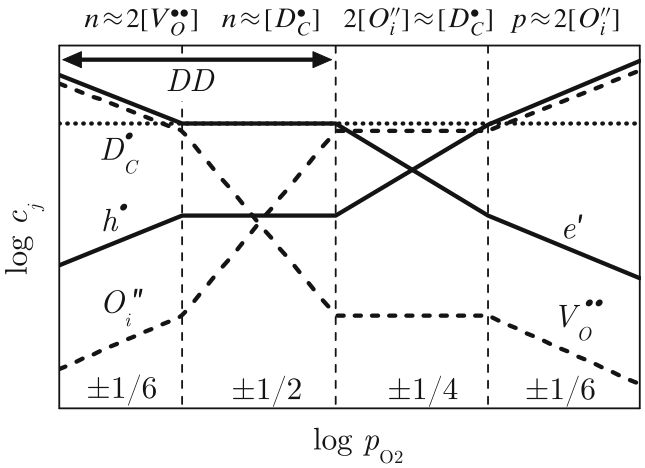

Fig. 31 Kröger–Vink diagram for net donor doped langasite and range of operation for donor doped (*DD*) langasite taken from [83]

4.2 Oxygen partial pressure ranges of operation

The p_{O2} ranges of operation of langasite must be explored with respect to the defect model. Section 3 provides the corresponding experimental results. The accessible p_{O2} (1–10^{-25} bar) and temperature ranges (700–1000°C) results from a comparison of the conductivity (Figs. 19–21) and the corresponding Kröger–Vink diagrams (Figs. 30 and 31). The following regions of operation denoted by *AD*, *UD* and *DD* are found:

- *AD* in Fig. 30 for acceptor (1% Sr) doped langasite.[5]
  Acceptor doped langasite exhibits mixed ionic-electronic conductivity. At low and medium p_{O2}, the charge transport is dominated by mobile oxygen vacancies. The ionic conductivity is fixed by the acceptors, thereby being p_{O2} independent. With increasing p_{O2} *p*-type electronic conduction takes over the bulk conductivity. The *n*-type conductivity is fully suppressed.
- *UD* in Fig. 30 for nominally undoped langasite.
  Nominally undoped langasite, prepared by ceramic processing routes, shows ionic conduction at medium and high p_{O2}. At low p_{O2}, *n*-type electronic conductivity becomes pronounced due to the generation of electrons by reduction. The situation corresponds to slightly acceptor doped material. As a consequence, the p_{O2} range of operation is shifted to lower values with respect to the intentionally acceptor doped material.
- *DD* in Fig. 31 for donor (5% Nb) doped langasite.
  Donor doped langasite is a *n*-type electronic conductor in the entire accessible p_{O2} range. At low p_{O2}, the generation of electrons leads to an increased conductivity with respect to the situation at medium and high p_{O2} where the electron concentration is fixed by the donor doping.

The analytical relations between p_{O2} and total conductivity summarized in Table 7 are restricted to the specific p_{O2} regions of operation mentioned above. As intermediate information, neutrality equations and dominating charge carriers in langasite are given for the experimentally accessible p_{O2} ranges.

So far, the discussion refers to the temperature and oxygen partial pressure dependence of the bulk conductivity. However, both types of dopants lead to

[5]The amount of dopant is always given as molecular percentage of the target cation site. Strontium and praseodymium dopants refer to lanthanum. Niobium dopants are given with respect to gallium.

Table 7 Dominating charge carriers in langasite for different net dopant types in the experimentally accessible p_{O2} range and conductivity of langasite as function of p_{O2}

p_{O2}	Nominally undoped[a] $[A'_C] > [D^{\bullet}_C]$		Acceptor doped $[A'_C] > [D^{\bullet}_C]$		Donor doped $[D^{\bullet}_C] > [A'_C]$	
	Neutrality	Conduction	Neutrality	Conduction	Neutrality	Conduction
Low		$n > [V^{\bullet\bullet}_O]$ $\sigma_e > \sigma_V$ $\rightarrow$ electronic $\sigma_B \sim p_{O2}^{-1/4}$			$n \approx 2[V^{\bullet\bullet}_O]$	$\mu_n > \mu_V$ $\sigma_e > \sigma_V$ $\rightarrow$ electronic $\sigma_B \sim p_{O2}^{-1/6}$
↓				$[V^{\bullet\bullet}_O] \gg n$ $\sigma_V > \sigma_e$ $\rightarrow$ ionic $\sigma_B \neq f(p_{O2})$		
Medium	$2[V^{\bullet\bullet}_O] \approx [A'_C]$		$2[V^{\bullet\bullet}_O] \approx [A'_C]$			
		$[V^{\bullet\bullet}_O] \gg n$ $\sigma_V > \sigma_e$ $\rightarrow$ ionic $\sigma_B \neq f(p_{O2})$				$n > [V^{\bullet\bullet}_O]$ $\sigma_e > \sigma_V$ $\rightarrow$ electronic $\sigma_B \neq f(p_{O2})$
↓				$p > [V^{\bullet\bullet}_O]$ $\sigma_e > \sigma_V$ $\rightarrow$ electronic $\sigma_B \sim p_{O2}^{1/4}$	$n \approx [D^{\bullet}_C]$	
High						

[a]Prepared by ceramic processing routes

regions of p_{O2} independent conduction determined by either oxygen vacancies or electrons. Consequently, conductivity measurements as function of p_{O2} by oneself are not suited to identify the predominant charge carrier in the entire p_{O2} range. Therefore, accompanying experimental methods are applied and presented in [80–82] to support the defect model. In particular, thermoelectric power and concentration cell measurements are performed to confirm sign and concentration of the dominant charge carriers and to determine reaction constants and mobilities.

4.2.1 Conductivity prediction

The detailed analysis presented in [80–82] enables, for example, to predict the bulk conductivity of langasite as a function of net dopant concentration $[A'_C] - [D^{\bullet}_C]$ for a given temperature. Figure 32 shows the results for 800 and 1000°C which follow essentially the same pattern.[6] As already mentioned, acceptor doped langasite exhibits mixed ionic-electronic conductivity with predominant ionic contributions. Consequently, a weak p_{O2} dependence of the conductivity is observed.

Donor doped langasite shows electronic conductivity at all p_{O2} leading to enhanced conduction at low p_{O2}. To reduce the conductivity to a minimum in air, a perfectly compensated langasite is required. This region is indicated in Fig. 32 by a gray bar. According to the slope of the curves around $[A'_C] - [D^{\bullet}_C] = 0$, it is, a priori, difficult to predict whether materials processing will result in a predominant ionic or electronic conductivity. For example, nominally undoped polycrystalline langasite prepared by ceramic processing routes, behaves like acceptor doped langasite. The fact applies not necessarily for single crystalline langasite prepared be the Czochralski technique.

The defect model predicts a relatively weak impact of the dopant concentration if the material is not perfectly compensated. Assuming for example $[A'_C] - [D^{\bullet}_C] = -1\%$, the increase of the acceptor concentration by 0.25% would decrease the conductivity by a factor of 0.84 (see Fig. 32). Donor doping by 0.5% would increase the conductivity by a factor of 1.18. Such changes are hardly measurable. The conductivity

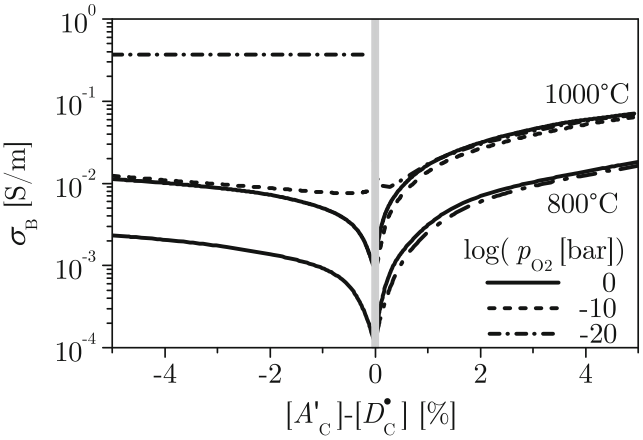

Fig. 32 Bulk conductivity prediction for langasite at different oxygen partial pressures at 800 and 1000°C as function of net dopant level taken from [83]

[6]At 800°C the curves for $p_{O2} = 1$ and 10^{-10} bar are almost identical. At 800°C and $p_{O2} = 10^{-20}$ bar the branch for $[A'_C] - [D^{\bullet}_C] < 0$ is not shown in order to avoid confusion because of overlapping curves. It is a nearly horizontal line at $\sigma_B \approx 6 \times 10^{-3}$ S/m.

change of niobium doped langasite goes along with the expected trend as seen in Fig. 25. The letter statement does not apply for praseodymium doped langasite. Therefore, it is under question, if praseodymium is ionized thereby acting as donor (see Table 6). In order to exclude the latter option, further attempts to dope langasite by donors are done using niobium. Its effect on the conductivity is already demonstrated in case of polycrystalline langasite.

In contrast, the conductivity prediction according to Fig. 32 points to an increase in conductivity by some orders in magnitude if langasite is highly acceptor doped. The expectation is confirmed by the measured change in conductivity of locally doped areas by three to four orders in magnitude as visualized in Fig. 25. The result confirms the effect of strontium doping predicted by the defect model. However, quantitative comparisons should not be given since the extrapolation of the conductivity prediction to high dopant levels as well as the determination of the conductivity of the doped area is a rough estimation, only.

Further, a homogenously doped langasite crystal containing only 0.5% Sr shows a considerable decrease in conductivity as visualized in Fig. 26. However, it cannot be decided whether the material is net donor or acceptor doped. The two branches for $[A'_C] - [D^{\bullet}_C] \lessgtr 0$ in Fig. 32 show identical conductivities for doping levels of different sign. The activation energy delivers the required information. The value of 1.39 eV for σT (see Table 4) indicates ionic conduction in the temperature range from 550 to 950°C since it corresponds roughly to the activation energy of the oxygen diffusion and the conductivity of strontium doped polycrystalline material.

Doping with 0.5% Nb results in a lower conductivity than undoped single crystals as seen in. Obviously, the material is effectively compensated. Remarkably, the activation energy of the conduction is lower than that of strontium doped langasite thereby indicating suppressed ionic conduction. The observation supports the defect model. As a consequence, the material is expected to show lower losses than nominally undoped or strontium doped langasite. The statement originates from the presumably stronger interaction of moving oxygen ions and lattice in comparison to that of electrons and lattice.

Further, the analysis in [80–82] includes a qualitative description of the oxygen vacancy concentration which enables to calculate mass changes of the resonator material. The formation of oxygen vacancies and electrons follows from the reaction constant according to Eq. 30

$$k_{R,A} = [V^{\bullet\bullet}_O]\, n^2\, p_{O2}^{1/2} = 10^{67} e^{-5.7\,\mathrm{eV}/k_B T}\ \mathrm{cm}^{-9}\,\mathrm{bar}^{1/2}. \quad (54)$$

for acceptor and

$$k_{R,D} = [V^{\bullet\bullet}_O]\, n^2\, p_{O2}^{1/2} = 10^{71} e^{-6.57\,\mathrm{eV}/k_B T}\ \mathrm{cm}^{-9}\,\mathrm{bar}^{1/2}. \quad (55)$$

for donor doped langasite, respectively. Changes in $[V^{\bullet\bullet}_O]$ can be calculated in concert with the general neutrality condition $2[V^{\bullet\bullet}_O] + [D^{\bullet}_C] = n + [A'_C]$ applying at low p_{O2}. The related mass change and the resulting frequency shift of langasite resonators are discussed in Section 5.

4.3 Hydrogen containing environments

The experimental results found in nominally hydrogen free atmospheres are consistent with the defect model presented so far. However, atmospheres containing substantial amounts of hydrogen lead to contradictions if the p_{O2} is lowered. In particular, the conductivity decreases with decreasing p_{O2} as shown by the corresponding experimental results in Section 3.4.

Hydrogenous atmospheres are created by H_2/H_2O gas mixtures where the amount of H_2 provided to the reaction chamber ($\sim p^{RT}_{H2}$) is kept constant. Thus the resulting hydrogen partial pressure p_{H2} at elevated temperatures $p_{H2} = p^{RT}_{H2} - p_{H2O}$ is reduced due to the formation of water vapor via $2\,H_2 + O_2 \rightarrow 2\,H_2O$. The equilibrium

$$p^2_{H2}\, p_{O2} / p^2_{H2O} = const. \quad (56)$$

results in

$$p^{\alpha}_{H2O} \sim p_{O2} \quad (57)$$

with $\alpha = 2$ in the marginal case of very low p_{O2}. With increasing p_{O2}, α becomes p_{O2} dependent and increases slightly.

Since langasite belongs to the same crystal class as α-quartz, similar impact of hydrogenous species is expected. In particular, the diffusion along the z-axis should be much faster than in other directions. Oxygen tunnels may be formed [93] where water reacts with e.g. Si-O-Si bonds. From the reaction of water incorporation into the crystal structure via

$$H_2O + O_O \leftrightarrow (2OH)_O, \quad (58)$$

the dependence of the conductivity along the z-axis as function of the water vapor partial pressure p_{H2O} is estimated to be

$$\sigma_Z \sim [(OH)_O] \sim p^{1/2}_{H2O}. \quad (59)$$

Equation 59 does not contains effectively charged particles. However, protons can migrate in the electrical field since the OH-groups are polar [94–96].

Further, hydrogen may react with e.g. Si-O-Si bonds according to

$$H_2 + O_O \leftrightarrow (H, OH)_O. \tag{60}$$

If both hydrogen atoms contribute to the charge transport in form of mobile protons, the mass action law and Eq. 56 result in

$$\sigma_Z \sim p_{H2O}^{1/4}. \tag{61}$$

For geometrical reasons, conduction of water through oxygen tunnels is not expected in the *y*-direction. Defect and transport mechanisms reported e.g. for perovskites [97] can be applied here. There, water incorporation relies on the existence of oxygen vacancies via the reaction

$$H_2O + V_O^{\bullet\bullet} + O_O \leftrightarrow 2(OH)_O^{\bullet}. \tag{62}$$

The conductivity depends on both, the water partial pressure and the concentration of oxygen vacancies

$$\sigma_Y \sim [(OH)_O^{\bullet}] \sim p_{H2O}^{1/2}[V_O^{\bullet\bullet}]^{1/2}. \tag{63}$$

At low temperatures, where $[V_O^{\bullet\bullet}]$ is frozen in or where $[V_O^{\bullet\bullet}]$ is fixed by acceptors,

$$\sigma_Y \sim [(OH)_O^{\bullet}] \sim p_{H2O}^{1/2} \tag{64}$$

is expected. With increasing temperature the concentration of oxygen vacancies at sufficiently low p_{O2} depends on the oxygen partial pressure according to $[V_O^{\bullet\bullet}] \sim p_{O2}^{-1/6}$ (see Eqs. 30 and 45). Using Eq. 57, the dependence of σ_Y from p_{H2O} follows

$$\sigma_Y \sim \left[(OH)_O^{\bullet}\right] \sim p_{H2O}^{1/2-\alpha/12}. \tag{65}$$

In the limiting case of very low p_{O2} from $\alpha = 2$ results

$$\left[(OH)_O^{\bullet}\right] \sim p_{H2O}^{1/2-0.17}. \tag{66}$$

For higher p_{O2} with $\alpha \gtrsim 2$ smaller exponents are expected.

Another option is the formation of protons at the surface of langasite according to

$$H_2 \leftrightarrow 2H^{\bullet} + 2e'. \tag{67}$$

In this case, the conductivity depends on the hydrogen partial pressure p_{H2} as follows

$$\sigma_Y \sim p_{H2}^{1/4} \tag{68}$$

and can be related to p_{H2O} using Eqs. 56 and 57

$$\sigma_Y \sim p_{H2O}^{1/4-\alpha/8}. \tag{69}$$

For very low p_{O2}'s ($\alpha = 2$) a p_{H2O} independent conductivity results if the latter reaction applies. With increasing p_{O2} ($\alpha > 2$) a negative exponent, i.e. decreasing conductivities with increasing p_{H2O} is expected (Table 8).

The appropriate reactions can be identified using the experimental data as presented in Section 3.4. Figure 28 indicate a 1/2 dependence of the conductivity along the *z*-axis at 800°C in the $\log(\sigma_B) - \log(p_{O2})$ plot. Thereby, the water incorporation according to Eq. 58 is confirmed. Further, the exponent at 600°C is very close to 1/2 as shown in Fig. 28. The observation supports Eq. 64 which describes the conductivity for fixed oxygen vacancy concentration. At 800°C, the exponent found in the experiment indicates an impact of the oxygen vacancy concentration. It corresponds to the predicted value for proton conduction for $\alpha = 3.6$ (see Eq. 65) and confirms the reaction according to Eq. 62. Numerous other tested models could not fulfill the experimentally determined p_{H2O}-dependence of σ_Y and the p_{H2}^{RT} independence of the conductivity. The latter becomes obvious by the different symbols in Fig. 28 which lie on a line for a given orientation and temperature.

Table 8 Potential reactions and corresponding p_{H2O} dependent conductivities of langasite

Direction	Reaction	Conductivity	Remark
z	$H_2O + O_O \leftrightarrow (2OH)_O$	$\sigma_Z \sim [(OH)_O] \sim p_{H2O}^{1/2}$	
	$H_2 + O_O \leftrightarrow (H, OH)_O$	$\sigma_Z \sim p_{H2O}^{1/4}$	
y	$H_2O + V_O^{\bullet\bullet} + O_O \leftrightarrow 2(OH)_O^{\bullet}$	$\sigma_Y \sim p_{H2O}^{1/2}$	Low temperature ($[V_O^{\bullet\bullet}] = const$)
		$\sigma_Y \sim \left[(OH)_O^{\bullet}\right] \sim p_{H2O}^{1/2-\alpha/12}$	high temperature ($[V_O^{\bullet\bullet}] \sim p_{O2}^{-1/6}$)
y	$H_2 \leftrightarrow 2H^{\bullet} + 2e'$	$\sigma_Y \sim p_{H2O}^{1/4-\alpha/8}$	high p_{O2} ($\alpha > 2$)
		$\sigma_Y = const.$	low p_{O2} ($\alpha = 2$)

5 Correlation of electromechanical properties and defect chemistry

5.1 Gas atmosphere dependent frequency

In order to take advantage of the high mass resolution of langasite resonators, atmosphere-independence of the resonance frequency must to be ensured. Therefore, this section focuses on mapping the regimes of gas insensitive operation of langasite resonators and the correlation to langasite's defect chemistry for temperatures up to 1000°C. For the discussion, frequency fluctuations equivalent to noise of ±4 Hz (see [3]) are taken as criterion to determine the p_{O2} range of stable operation.

5.1.1 Nominally hydrogen free atmospheres

First, CO/CO_2 atmospheres are regarded since additional mass loads are expected due to the incorporation of hydrogen or OH-groups. In the absence of hydrogen, the most relevant feature of the defect model vis-a-vis analysis of resonator operation is the formation of oxygen vacancies $[V_O^{\bullet\bullet}]$ at low p_{O2}.

In case of net acceptor concentration $[A'_C] > [D^{\bullet}_C]$, the concentration of oxygen vacancies is fixed according to Eq. 46 by $2[V_O^{\bullet\bullet}] \approx [A'_C]$ at high p_{O2}. Consequently, mass and frequency of langasite resonators are expected to be constant. With decreasing p_{O2}, the reduction reaction controls the concentration of electrons and oxygen vacancies. Based on the neutrality condition $2[V_O^{\bullet\bullet}] = n + [A'_C]$ and the reaction constant according to Eq. 54, changes in $[V_O^{\bullet\bullet}]$ are calculated and converted into a fractional density change $(\Delta\rho_R/\rho_R)$ by relating the mass of formed $[V_O^{\bullet\bullet}]$ $(\sim \Delta\rho_R)$ and the mass of the resonator material $(\sim \rho_R)$. The corresponding frequency shift Δf is calculated using Eq. 17. For $[..] = \rho_R$ the numerical approach described in Section 2.7 yields $\kappa_\rho = -1/2$. The result is visualized in Fig. 33 for $f = 5$ MHz.

At 1000°C, the calculated frequency shift exceeds the limit of ±4 Hz below $p_{O2} = 10^{-17}$ bar, whereas resonators are expected to be stable down to 10^{-24} and 10^{-36} bar at 800 and 600°C, respectively. Figure 33 shows further that the mass change, i.e. the formation of oxygen vacancies, already begins $(\Delta[V_O^{\bullet\bullet}] > 10^{15}$ cm$^{-3})$ at about 10^{-5} and 10^{-14} bar at 1000 and 800°C, respectively. In contrast, the oxygen vacancy concentration remains unchanged $(\Delta[V_O^{\bullet\bullet}] < 10^{15}$ cm$^{-3})$ down to 10^{-25} bar at 600°C (not shown in Fig. 33). In case of net donor doped langasite, a similar approach can be followed and results in a slightly smaller range of independent operation (dashed lines in Fig. 33).

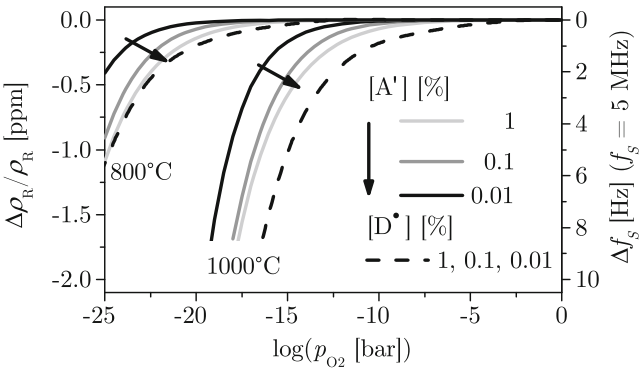

Fig. 33 Calculated relative mass change and frequency shift of 5 MHz langasite resonators as function of oxygen partial pressure for different acceptor and donor concentrations at 800 and 1000°C

5.1.2 Hydrogen containing atmospheres

So far, the impact of hydrogenous species on the conductivity is presented. The reaction according to Eq. 62 includes the incorporation of OH-groups. Therefore, frequency shifts related to the resonator density are expected. Under the experimental conditions chosen here, p_{H2O} is fixed $(\Delta \log(p_{H2O}[\text{bar}] < 10^{-3})$ due to the H_2/H_2O buffer above $p_{O2} \approx 10^{-20}$ and 10^{-13} bar at 600 and 800°C, respectively. Therefore, a constant frequency is expected above that p_{O2}'s.

The frequency shift is investigated experimentally by tracing the resonance frequency for $p_{O2} = 10^{-6}$–10^{-25} bar at 600°C. Thereby, a 2.1 MHz resonator is used. The observed resonance frequency shift $\Delta f_{2.1} = f_{2.1}(p_{O2}) - f_{2.1}(p^0_{O2})$ is converted into values for 5 MHz resonators Δf by

$$\Delta f(p_{O2}) = \frac{5\text{ MHz}}{f_{2.1}(p^0_{O2})}\Delta f_{2.1}(p_{O2}) \tag{70}$$

thus enabling a direct comparison with the 5 MHz resonators. Thereby, p^0_{O2} is chosen to be 10^{-10} bar. The result is shown in the upper part of Fig. 34. The resonance frequency remains constant above about $p_{O2} = 10^{-20}$ bar. Below that p_{O2}, the resonance shifts to higher frequencies. At $p_{O2} = 10^{-25}$ bar, $\Delta f \approx 1200$ Hz is found. The change occurs at a p_{O2} significantly higher than $p_{O2} = 10^{-36}$ bar which is the lower limit of constant conductivity in CO/CO_2 atmospheres at 600°C. The fact indicates a minor impact of mechanisms which determine the conductivity under these circumstances. In particular, the concentration of oxygen vacancies $[V_O^{\bullet\bullet}]$ is expected to be virtually constant.

A detailed discussion requires the separation of the materials parameter related contributions to the

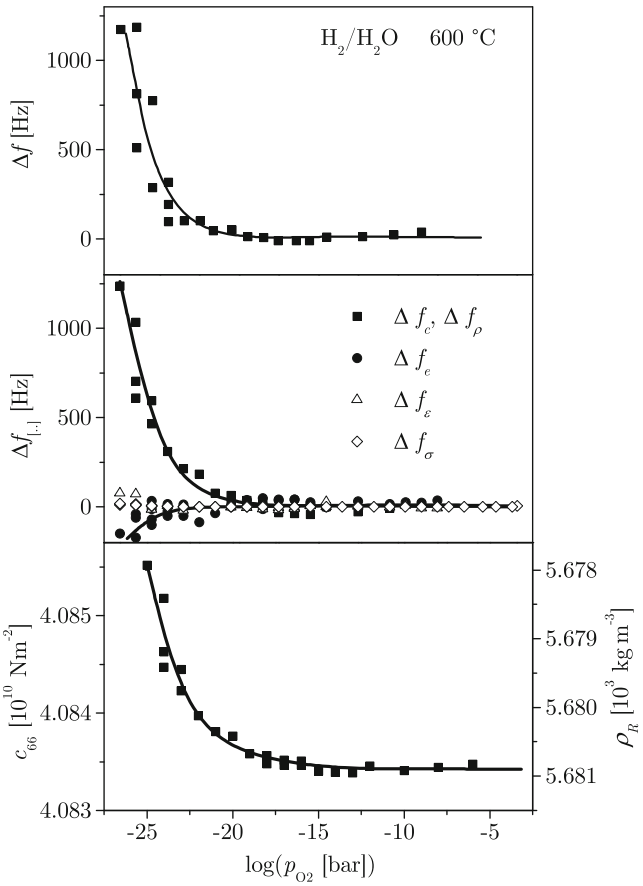

Fig. 34 Resonance frequency shift (*top*), materials parameters related frequency shift contributions (*center*), shear modulus and density (*bottom*) as function of p_{O2} in hydrogen containing atmospheres at 600°C. Note the inverse scale for ρ_R

frequency shift. For that purpose, the resonance spectra are analyzed using the one-dimensional physical model. First, the BvD parameters are extracted and converted into the materials parameters as described in [3]. Intermediate results are their relative changes $\Delta[..]/[..]$ as function of p_{O2}. Secondly, Eq. 16 is rewritten to determine the frequency shift

$$\Delta f = \frac{\partial f}{\partial [..]} \Delta [..] = f \kappa_{[..]} \frac{\Delta [..]}{[..]}. \tag{71}$$

The calculation refers to 5 MHz resonators, i.e. f is chosen to be 5 MHz. The values of the relative derivatives $\kappa_{[..]}$ required for the calculation result from the numerical approach described in Section 2.7. The values given for 500° in Fig. 12 correspond roughly to those at 600° used here. It must be noted that frequency shifts related to changes in shear modulus and density cannot be separated. The fact becomes obvious from Eq. 63 in [3]. Therefore, the calculation is initially done for $\rho = const$. The related change in density follows from

$$\rho_R\left(p_{O2}\right) = \rho_R\left(p^0_{O2}\right) \frac{c_{66}\left(p^0_{O2}\right)}{c_{66}\left(p_{O2}\right)}. \tag{72}$$

The central part of Fig. 34 shows the frequency shift caused by the p_{O2} dependence of the materials parameters. The result indicates a predominant impact of c_{66} or ρ_R. Changes caused by the other materials parameters are almost negligible (σ_R and ε_R) or small (e_R). Table 9 presents the numerical results, since accurate numbers cannot be taken from the plots.

Finally, the question must be discussed whether changes in shear modulus or density determine the frequency shift predominantly. The left and right hand scale in the bottom part of Fig. 34 indicate their p_{O2}-dependence, respectively, if the other property is fixed.

According to Eq. 62, H_2O is removed from the lattice with decreasing p_{H2O}. The situation corresponds to decreasing p_{O2}'s. Consequently, the calculated decrease in density goes along with the model which is already confirmed by the p_{H2O}-dependence of the conductivity (Fig. 28). Further, from $\Delta\rho_R/\rho_R = -5.2 \times 10^{-4}$ follows $\Delta n_{H2O} \approx -10^{20}$ cm^{-3} which requires the existence of about 10^{20} oxygen vacancies per cm^{-3}. The latter sounds about reasonable with respect to

- The oxygen sites available in langasite (5×10^{22} cm^{-3}) and
- The oxygen vacancy concentration reported in [39] for nominally undoped single crystalline langasite of 10^{19} cm^{-3}.

Based on these insights, the frequency shift can be described by the removal of OH-groups at low p_{O2}. The model is in accordance with conductivity changes which makes it a likely explanation. However, an impact of p_{O2} on the shear modulus can not be excluded entirely.

At 800°C, density changes and related frequency shifts are expected be even stronger. More important, 5 MHz langasite resonators are already operated close to its dielectric relaxation frequency. Consequently, the impact of conductivity changes on the resonance frequency becomes pronounced. With $\kappa_\sigma = -5.5 \times 10^{-4}$ and $\Delta\sigma/\sigma = 0.19$ follows $\Delta f = -522$ Hz. Such frequency shifts prevent the application of langasite resonators as resonant sensors. Consequently, operation frequencies far off the dielectric relaxation frequency have to be chosen (see also Section 5.2).

As discussed in Section 3, the calculated frequency shift induced by redox related reactions in nominally hydrogen free atmospheres only exceeds the limit of ±4 Hz at fairly low p_{O2}'s. Water vapor is found to

Table 9 Relative derivatives of the materials properties, relative changes in materials properties and absolute frequency shift contributions of 5 MHz resonators for changes in p_{O2} from 10^{-10} to 10^{-25} bar in hydrogen containing atmospheres at 600°C

[..]	c_{66}	(ρ_R)	e_R	ε_R	σ_R
$\kappa_{[..]}$	0.5	(−0.5)	6.2×10^{-3}	-3.1×10^{-3}	-8.2×10^{-6}
$\Delta[..]/[..]$	5.2×10^{-4}	(-5.2×10^{-4})	-6.1×10^{-3}	-5.3×10^{-3}	3.8×10^{-2}
Δf (Hz)	1300	(1300)	−190	82	−2

shift the resonance frequency already at higher p_{O2}'s. In the hydrogen containing atmospheres applied here, langasite can be regarded as a stable resonator material above oxygen partial pressures of about 10^{-20} and 10^{-13} bar at 600 and 800°C, respectively.

5.2 Correlation of loss and conductivity

5.2.1 Dielectric relaxation frequency

Mechanical losses include contributions related to the electrical conductivity. Piezoelectric coupling causes this impact of electrical properties as already mentioned in Section 2.2. Its maximum is found at the (angular) dielectric relaxation frequency $\omega_\varepsilon = \sigma_R/\varepsilon_R$. The corresponding frequency $f_\varepsilon = \omega_\varepsilon/(2\pi)$ for nominally undoped langasite is denoted by $f_\varepsilon(\sigma_R)$ in Fig. 35. Any operation frequency off that curve is advantageous since the contribution of the conductivity to the mechanical loss would be low.

Further, the resonance frequency is influenced by the conductivity in the vicinity of the dielectric relaxation frequency. Detailed insights provide the relative derivatives κ_σ in Fig. 12. A temperature difference ΔT of at least 250 K between maximum (at 925°C) and small impact (below 675°C) of the conductivity

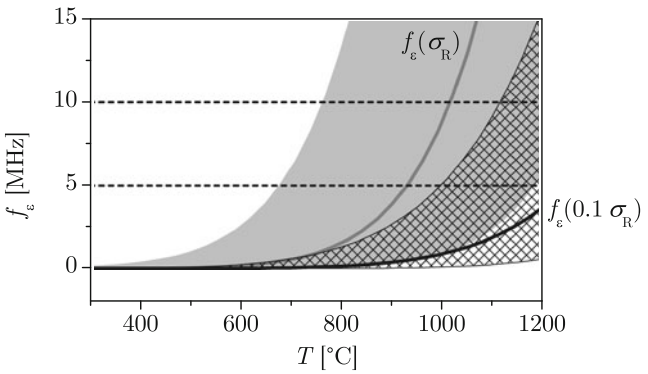

Fig. 35 Dielectric relaxation frequency f_ε calculated for the conductivity of nominally undoped langasite ($f_\varepsilon(\sigma_R)$) and for a conductivity reduced by a factor of 10 ($f_\varepsilon(0.1\,\sigma_R)$). The corresponding ranges of pronounced conductivity related frequency shifts are indicated by the gray and hatched area, respectively

can be estimated. Assuming the same temperature difference of ±250 K for other operation frequencies than 5 MHz, the unfavorable range of conductivity affected resonance frequencies follows. It corresponds to the gray area in Fig. 35. For example, 5, 10 and 15 MHz resonators should be used up to about 675, 760 and 810°C, only. Consequently, the choice of an increased resonance frequency does not increase the recommended temperature limit significantly. One option to overcome the problem is to modify the conductivity as presented in Section 3.4. For a conductivity reduced by a factor of 10 with respect to nominally undoped langasite, the dielectric relaxation frequency denoted by $f_\varepsilon(0.1\,\sigma_R)$ in Fig. 35 is calculated. The corresponding range of strongly conductivity affected frequencies is given by the hatched area. The effect of the decreased conductivity is clearly obvious. The recommended operation temperatures are shifted to significantly higher values, namely 1000, 1110 and 1185°C for 5, 10 and 15 MHz resonators, respectively.

Thinking reverse, low frequency resonators can be operated at temperatures above the unfavorable range. For example, 5 MHz resonators are expected to be usable again above about 1200°C. As seen in Fig. 35, at this temperature the above mentioned frequency is already outside the unfavorable range around the dielectric relaxation frequency (gray area). Despite of increased total losses, the approach is reasonable since the conductivity related loss dominates the overall behavior above about 650°C (see Fig. 37). Here, the increase of bulk conductivity does not increase the bandwidth of the resonance spectrum if expressed as admittance. The fact becomes obvious by regarding the static admittance G_S ($\sim 1/R_S$) which shifts the entire resonance spectrum. (For details see Section 4.4.2 in [3].) Therefore, the frequency determination by network analysis is still feasible. In practice, the overall loss, expressed as the inverse Q-factor, tends to decrease above about 1000°C as seen in Fig. 37. Thin film platinum electrodes prevent test temperatures above 1050°C. Calculations for 5 MHz resonators using extrapolated materials properties of langasite (see Section 2.6) result in Q-factors of about 50 at 1400°C. Resonators wearing lanthanum strontium manganate (LSM) electrodes are used for comparison. Those films

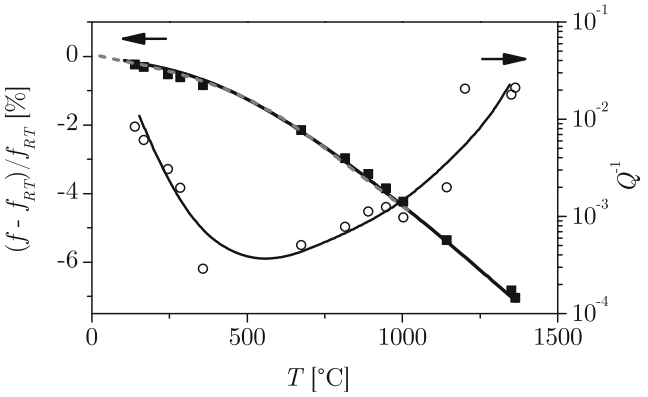

Fig. 36 Temperature dependent resonance frequency and resonator quality factor of a 5 MHz langasite resonator wearing LSM electrodes

become sufficiently conductive above about 500°C. Most remarkably, 5 MHz langasite resonators wearing LSM electrodes show Q-factors of about 50 at 1350°C (Fig. 36).

5.2.2 Dominating loss parameter

The Q-factor for langasite is derived from the parameters of the equivalent circuit according to Eq. 13 and compared with the viscosity as shown in Fig. 37. Appropriate scaling of the left and right hand axis demonstrates their equivalence up to about 550°C for langasite. Above that temperature, langasite is influenced by conductivity related losses. The transition temperature can be defined by the condition $Q^{-1} = 2\,Q_{\eta}^{-1}$ leading to about 650°C. For comparison, the data for $GaPO_4$ and quartz are given which match in the entire respective temperature range.

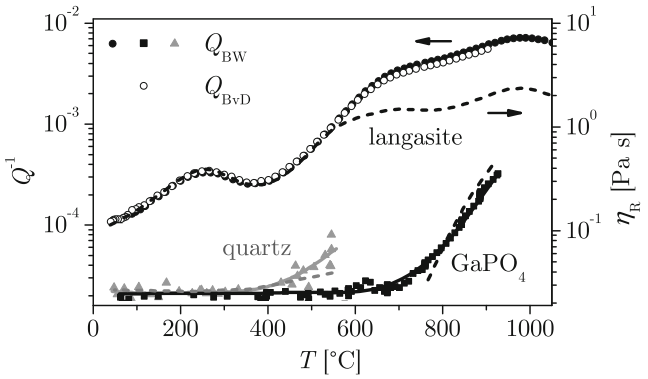

Fig. 37 Inverse Q-factor (*solid lines* and *symbols*) and viscosity (*dashed lines*) as function of temperature for langasite, gallium phosphate and quartz

5.2.3 Activation energies of loss and conductivity

In this section, the activation energies of loss and conductivity are compared in order to evaluate if both properties are determined by the same microscopic mechanism. Initially, the temperature range appropriate for that comparison must be identified.

(1) Room temperature to 350°C.
A local loss maximum is observed at about 250°C (see Fig. 37). The extend of the peak depends on the thermal history of the sample as also reported in [66, 98]. Further, the observation is in general agreement with results presented in [99]. An activation energy of 0.34 eV for point-defect relaxation and an Arrhenius like background behavior with an activation energy of 0.1 eV are reported at temperatures up to about 350°C. This loss peak is of minor interest for this work since other mechanisms overwhelm its effect at high temperatures.

(2) 350–650°C.
The loss is governed by the viscosity. However, the previously described loss peak influences the slope of the viscosity in this temperature range. The situation is shown schematically in the inlay of Fig. 38. At some elevated temperature, the curve for η appears to be nearly linear in the Arrhenius plot.[7] With decreasing temperature, the curve becomes flatter. A temperature independent contribution η_0 can be subtracted which results in an Arrhenius like behavior of $\eta - \eta_0$. This contribution is interpreted as sum of losses applying in range (1) and losses caused by imperfect resonator design, manufacturing, electrodes and mounting. An analogous subtraction of the background loss is chosen in [99] and [72] for langasite and quartz, respectively.[8]
The modified viscosity $\eta - \eta_0$ is not impacted by either background contributions, conductivity related mechanical loss or bulk conductivity and enables to extract the activation energy of the dominant mechanism as done at the end of this section.

(3) 650–1050°C.
The loss is governed by several parameters, i.e. viscosity, conductivity related mechanical loss and

[7] The subscript of η_R is skipped in this section.

[8] In both publications, the inverse resonator quality factor is used to describe the loss.

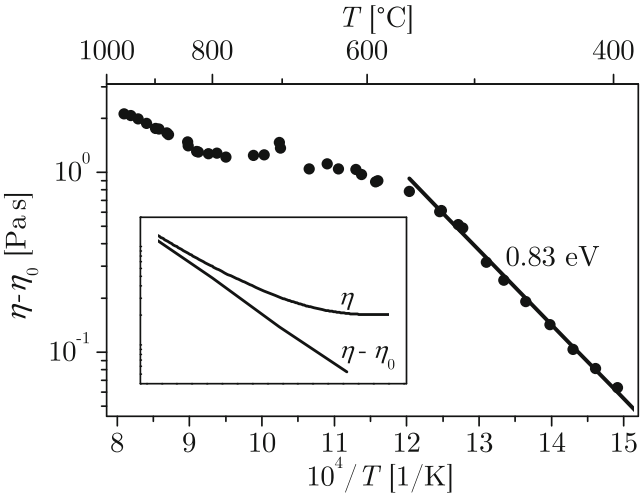

Fig. 38 Viscosity of undoped langasite without its temperature independent contribution and scheme of the viscosity with (η) and without ($\eta - \eta_0$) its temperature independent contribution η_0 (inlay)

bulk conductivity. Thus, a single activation energy cannot be extracted.

In summary, the intended comparison of the activation energies can be done only in the temperature range from 350 to 650°C where the loss is determined solely by the viscosity.

Figure 38 presents $\eta - \eta_0$ as function of the inverse temperature and the related activation energy. The value of 0.83 eV corresponds very well to that of the conductivity (see Table 10). Consequently, it is highly likely that the predominant conductivity mechanism also controls mechanical loss in temperature range (2). Based on the apparent correlation of conductivity and viscosity, lowering the electrical conductivity should result in lowering of damping and is, therefore, desirable. The latter conclusion applies in range (3) without any restrictions since conductivity related losses dominate (see Fig. 37).

Table 10 Activation energy of viscosity and conductivity in langasite

Langasite	Property	E_A [eV]	Temperature range [°C]
sc	σ_B	0.82	400–700
	$\eta - \eta_0$	0.83	400–600
sc (0.5% Nb)	σ_B	0.91	400–550
	$\eta - \eta_0$	0.95	420–580
sc (0.5% Sr)	$\sigma_B T$	0.98	400–550
	$\eta - \eta_0$	0.83	400–600

5.2.4 Strontium and niobium doped langasite

The effect of dopants on the loss is discussed separately for temperature ranges (2) and (3).

(2) 350–650°C.
Figure 39 presents the corrected viscosities $\eta - \eta_0$ of nominally undoped, strontium and niobium doped langasite. Niobium doped langasite exhibits a decreased viscosity and, therefore, a decreased loss with respect to undoped langasite. Contrary, strontium doped langasite does not show any change in viscosity. The observation must be discussed in concert with the conductivity of the differently doped crystals. They exhibit about the same change with respect to undoped langasite as seen in Fig. 26. Consequently, decreased conductivities go along with decreased losses in case of donor doping, only. In other words, the suppression of oxygen vacancies by donors decreases the loss. The observation confirms the expected stronger interaction of moving oxygen ions and lattice in comparison to that of electrons and lattice. Most remarkably, minimized losses do not require generally minimized total conductivity. In particular, the ionic contribution must be lowered in temperature range (2).
Further, similar activation energies of σ_B and $\eta - \eta_0$ are observed for undoped and niobium doped langasite, respectively. The statement becomes obvious from the numerical values summarized in Table 10. The fact indicates the control of both

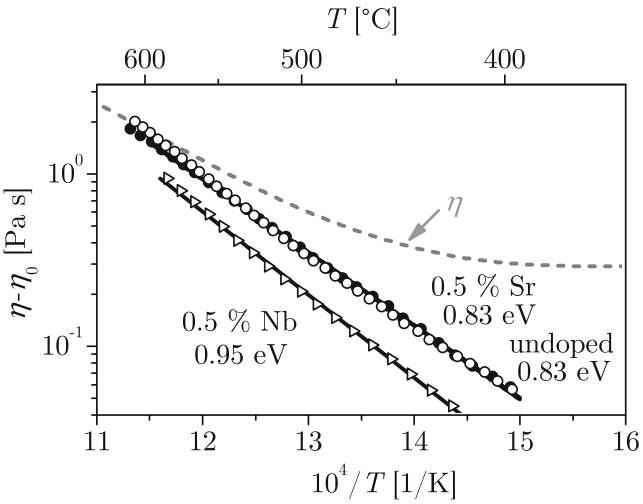

Fig. 39 Viscosity of nominally undoped, strontium and niobium doped langasite without its temperature independent contribution

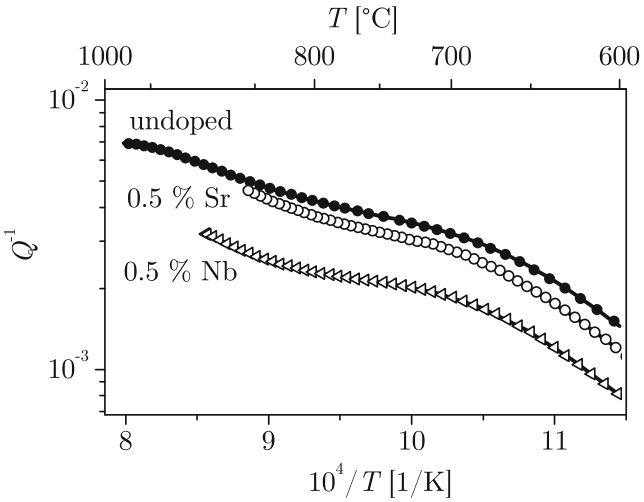

Fig. 40 Resonator quality factor of undoped, strontium and niobium doped langasite

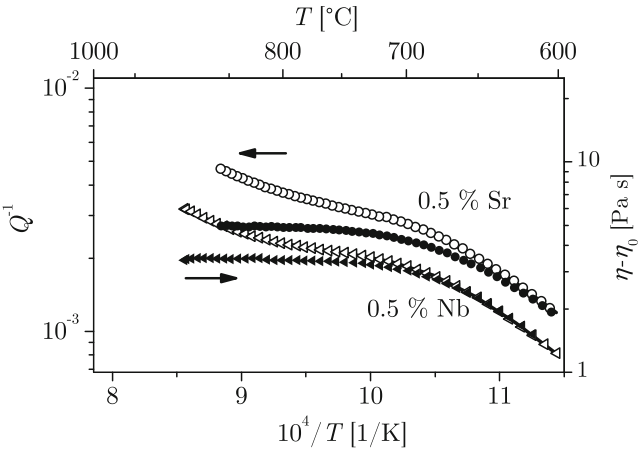

Fig. 41 Resonator quality factor (Q, *open symbols*) and viscosity ($\eta - \eta_0$, *solid symbols*) of strontium and niobium doped langasite

processes by the same mechanism. Contrary, the activation energies of $\sigma_B T$ and $\eta - \eta_0$ differ in case of strontium doped langasite thereby indicating different mechanisms.

(3) 650–1050°C.
In temperature range (3), the loss is described by the (inverse) Q-factor since the sum of different loss phenomena has to be regarded. Figure 40 compares the loss of undoped and doped langasite. Strontium doping decreases the loss slightly whereas niobium doping causes strong lowering of loss. The observed pattern in magnitude corresponds to that of the conductivity in temperature range (3) as presented in Fig. 26. Consequently, lowering the conductivity results generally in decreased losses. The latter statement corresponds to the dominance of conductivity related losses in the actual temperature range for undoped langasite. The validity of the statement for doped langasite can be seen from the comparison of Q^{-1} and $\eta - \eta_0$ as presented in Fig. 41.[9] The results indicate the dominance of conductivity related loss above about 650 and 700°C for strontium and niobium doped langasite, respectively.

6 Application relevant studies

Application relevant studies are performed in parallel to the investigation of the electromechanical properties and defect chemistry presented so far. The following sections summarize this results thereby underlining the application capabilities of high-temperature stable piezoelectric materials. The corresponding details are described in the references given below.

6.1 Micro-electromechanical structures

The availability of large size langasite wafers enables micromachining of this high-temperature stable piezoelectric material. Special emphasizes is taken on the development of monolithic structures to overcome problems originating from thermal stress. The concept includes the local doping of langasite by niobium, strontium and praseodymium. The doping is expected to result in locally increased conductivities to form electrodes. Another anticipated effect is the modification of the rate of wet chemical etching and, thereby, the option to etch the material locally.

To demonstrate the etching process and the potential of langasite as substrate for bulk micro-machining, micro-cantilever beams [100, 101] and membranes [102, 103] are designed and structured. As an example, the depth profile of a biconvex membrane is shown in Fig. 42. Such membranes exhibit higher Q-factors than the planar membrane type.

Further, the temperature dependent resonance frequency and Q-factor of an about 23 μm thick langasite membrane are given in Fig. 43. Due to the high resonance frequency, such membranes are operated far above their dielectric relaxation frequency (see Fig. 35) leading to relatively low electrical losses. Nevertheless, the resulting Qf-product of 4.7×10^{10} Hz at room temperature is lower than that for conventional 5 MHz resonators which can reach Qf-values of 10^{12} Hz. The

[9] The alignment of the left and right hand axis is done for data points in temperature range (2) where the viscosity dominates the loss solely (see also Fig. 37).

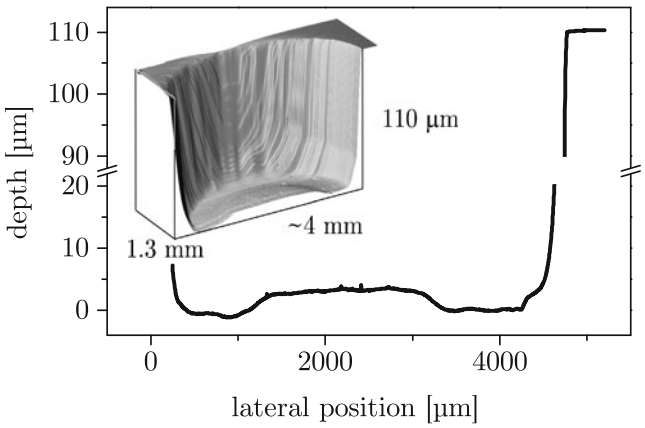

Fig. 42 View and depth profile of a langasite membrane prepared by wet chemical etching

fact can be explained by the ignorance of some design rules [56]. Diameters of 3 and 1.5 mm for the membrane and the electrode, respectively, are not the optimum. Smaller electrodes should result in higher Qf-products.

Taking the materials data of langasite at 600°C, the mass sensitivity $S = 2f^2/\sqrt{c_{66}/\rho}$ [3] results for 60 MHz resonators in a very high value of 4.6 cm^2 Hz/ng. In comparison, 5 MHz langasite or quartz resonators which show a mass sensitivity of 0.033 cm^2 at 600°C or 0.056 cm^2 Hz/ng at RT, respectively [104]. The mass sensitivity of 60 MHz membranes enables, in particular, to monitor the absorption of sub-monolayers of gas particles and thereby gas sensing.

6.2 Monolithic electrodes

Thin film platinum electrodes used in this work are prepared by pulsed laser deposition. They impact the resonance behavior very little due to their thickness of typically 200 nm, only. However, evaporation of volatile platinum suboxides and agglomeration of platinum [105] are a major concerns if thin films are used. As a consequence, the operation temperature is limited to about 1000°C. Mesh-printed platinum electrodes can be used at higher temperatures. Such films are significantly thicker which results in less pronounced relative changes of their properties for a given period of time and temperature. However, the fundamental problem of platinum loss is not solved. Further, differences in thermal expansion of e.g. platinum electrodes ($\alpha_{Pt} = 8.8 \times 10^{-6}$ K^{-1} [44]) and langasite substrates ($\alpha_{x-LGS} = 5.1 \times 10^{-6}$ K^{-1}, $\alpha_{z-LGS} = 3.6 \times 10^{-6}$ K^{-1} [106]) result in mechanical stress which affects the thermal stability of the electrodes and of small langasite structures.

In order to minimize or exclude the mechanical stress, the metallic electrodes are replaced by monolithic electrodes in form of heavily strontium doped areas in langasite. They are prepared by thermal diffusion of strontium into langasite single crystals [103]. Such electrodes show a strongly increased conductivity (see Fig. 25) and are used to operate BAW resonators at elevated temperatures in ambient air. The inlays of Fig. 44 show the extent of the Sr-doped areas used for the tests and the Pt-contacts which are added outside of the oscillating area to connect external wires. Further, a reference resonator without Sr-doped areas, but with comparable Pt-contacts outside of the resonating area, is prepared and characterized. Resonance spectra are obtained by impedance spectroscopy as function of temperature. The resonator with monolithic electrodes shows a Qf-product of 2.8×10^{10} Hz at room temperature and of 1.5×10^9 Hz at 700°C.

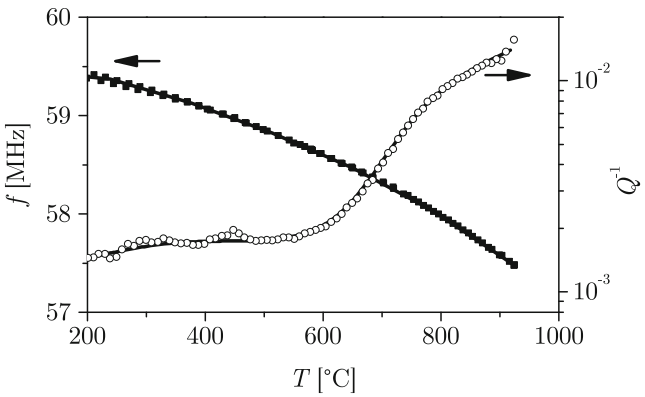

Fig. 43 Temperature dependent resonance frequency and resonator quality factor of an about 23 µm thick langasite membrane

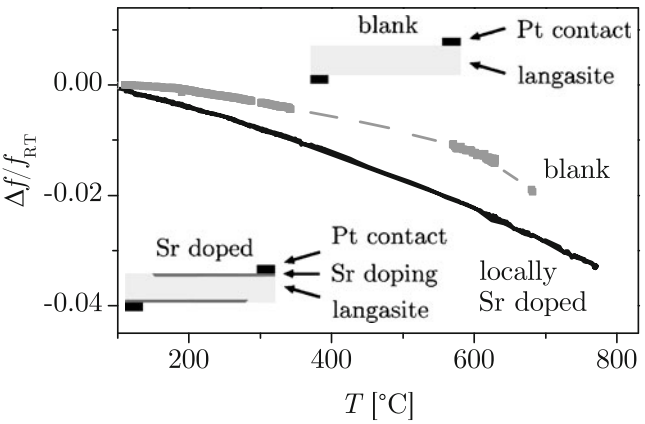

Fig. 44 Temperature dependent resonance frequency of a resonator with monolithic electrodes

6.3 Field emitter tips

Langasite structures of dimensions below 1 μm can be prepared using the above mentioned anisotropic etching process. The approach is applied to prepare field emitter tips as seen in the inlay of Fig. 45. Crystal faces and, thereby, sharp tips are formed due to the anisotropic etch process. Subsequently, they are used to demonstrate the operation of active electronic components. In order to decrease the work function of the surface, the tips are coated with platinum and installed. In order to test the devices, the tips are installed in a tube furnace which can be evacuated down to about 10^{-8} bar. The field emitting characteristics are determined using an electrometer (Keithley 6517A) using an internal voltage supply of ±1000 V.

Figure 45 shows the current as function of the applied voltage at room temperature. Here, the typical characteristics of a field emitting diode becomes obvious. Only positive voltages result in an exponential increase in current. A significant current is observed above about 400 V which reaches 67 μA at 1000 V. The field emission current can be described by the Fowler–Nordheim equation [107, 108]. A linear slope of the data in the corresponding plot reflects the occurrence of field emission and enables to calculate the radius of the tip. For the actual device a radius of only 27 nm is found.

At elevated temperatures the current-voltage characteristic changes slightly due to an ohmic contribution of langasite. The latter is visible at lower voltages, only. At higher voltages the field emission is dominating and determines the diode characteristics. The effect is demonstrated up to 600°C. Here, the emission of thermal electrons can be neglected. Further, the maximal current is decreased to about 70 nA at 510°C. Since the slope in the Fowler-Nordheim plot remains unchanged, the decreased current is ascribed to a lower emitting area of the tip. The latter is attributed to partial covering of the tip by gas particles due to the increasing residual pressure in the test chamber with increasing temperature.

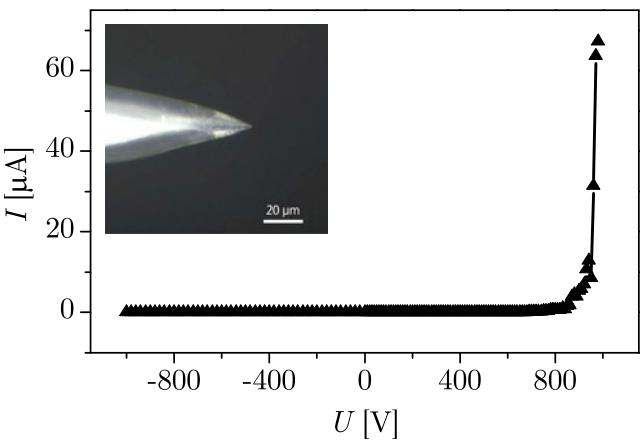

Fig. 45 Field emission current extracted from a langasite tip at room temperature

6.4 Gas sensor applications

In this section the gas sensing capabilities of sensor film coated langasite resonator devices at 600°C are demonstrated. It is already shown that the electromechanical properties of undoped langasite are suited for the operation of 5 MHz resonators at this temperature.

Stoichiometry changes induced in metal oxide films and related surface adsorption phenomena can be used for gas sensing at elevated temperatures. Variations in the composition of the surrounding gas atmosphere are expected to influence simultaneously the mechanical and electrical properties of the sensor film, in particular its mass, and its electrical conductivity (see [3]) thereby providing often orthogonal information about the gas. In order to increase the gas selectivity, the simultaneous measurement of changes in mechanical and electrical sensor film properties is desirable.

The effect of both properties is detected using $TiO_{2-\delta}$ coated langasite resonators with specially adapted electrode geometries. Platinum electrodes with different diameters are deposited on the opposite faces of the resonators as schematically shown in the upper part of Fig. 46. Thereby, resonator (M) is operated in the conventional microbalance mode. Changes in $TiO_{2-\delta}$ conductivity do not influence the resonance behavior since the underlying platinum electrode is larger than the platinum film. Contrary, resonator (E) reflects changes in the $TiO_{2-\delta}$ conductivity due to its influence on the effective electrode size. In this case, the $TiO_{2-\delta}$ film exceeds the underlying platinum electrode. The electrode layout and the related effects are explained in detail in [3, 109].

The existence of a combined conductivity and mass related sensor response motivates the attempt to distinguish between CO and H_2 containing gases. Figure 46 presents temperature-compensated frequency shifts Δf_{IC} obtained as a function of the oxygen partial pressure at about 600°C for gas mixtures of H_2/H_2O and CO/CO_2 with Ar as buffer gas. While the response of resonator (E) appears to be influenced only by the p_{O2}, resonator (M) reflects the type of gas. In practice, where the p_{O2} is unknown, the signal of resonator (E) has to be used to acquire this information. Most important, the different slope and magnitude

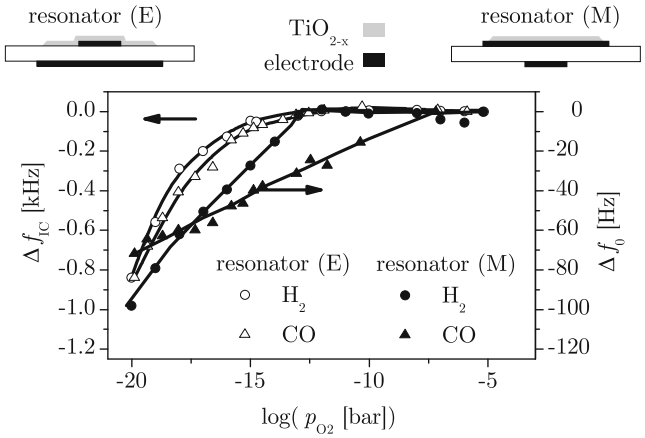

Fig. 46 Resonance frequency of $TiO_{2-\delta}$ coated langasite resonators with different electrode design as function of oxygen partial pressure at 600°C in different H_2/H_2O and CO/CO_2 containing atmospheres

of the frequency shift of both resonators enables the detection of CO in hydrogen containing atmospheres in the p_{O2} range from 10^{-13} to 10^{-20} bar. Further investigations include other sensor film materials such as CeO_2 which enable gas detection at higher p_{O2}'s [110].

7 Conclusions

A one-dimensional physical model is summarized which describes the electromechanical behavior of thickness shear mode resonators at elevated temperatures. Finite lateral dimensions of such devices require the introduction of areas which reflect the effective amplitude of the mechanical vibration and the effective electrode area. Most remarkably, both areas differ by a factor of about two. The accurate description of high-temperature resonators must consider this fact. Further, the physical model includes losses in form of imaginary parts of the materials constants. The analysis of the resonance spectra showed that the loss in langasite can be described satisfactorily by the mechanical and electric contributions expressed as effective viscosity and finite bulk conductivity, respectively. A parameter study is performed to evaluate the impact of the materials properties on the resonance behavior. The expressions developed can be regarded as generalized Sauerbrey equations. Properties most relevant for environmentally dependent frequency shifts and losses are identified to be shear modulus, density, electrical conductivity and effective viscosity.

The contribution of viscosity and conductivity to the total loss is analyzed. The essential result is the appearance of three distinct temperature ranges dominated by mechanical losses related to the viscosity, mechanical losses related to the electrical conductivity and electric losses. Most remarkably, the mechanical loss is significantly impacted by the electrical conductivity due to the piezoelectric coupling. That loss contribution shows a maximum which is found at the dielectric relaxation frequency. Minimization of the conductivity or the resonator operation off that frequency is recommended. Data of langasite indicate dominant viscoelastic losses up to about 650°C while the dielectric loss dominates about that temperature. The loss peak related to the piezoelectric coupling is observed at about 900°C for 5 MHz resonators.

In order to explore the operation limits and options to improve the resonance properties of langasite its defect chemistry is investigated. Thereby, a defect model developed using polycrystalline langasite is found to be valid for single crystals. Most remarkably, the electrical conductivity of nominally undoped langasite prepared by the Czochralski technique is dominated by *n*-type electronic carriers below 700°C and turns in predominant oxygen ion conduction above that temperature. The activation energy of the oxygen diffusion is found to be higher than that of the electronic conduction and almost equal to the activation energy of the total conductivity above 700°C. The former statements apply for high oxygen partial pressure. With decreasing oxygen partial pressure *n*-type electronic conduction becomes always dominant, e.g. below 10^{-24} bar at 800°C. Mobile anions do not impact the electrical conductivity as verified by measurements of the gallium diffusion.

Moving oxygen ions are always present even if they do not govern the electrical conductivity. Therefore, their presumably strong effect on damping is expected also at low temperatures. Consequently, donor doping appears to be always appropriate to decrease the loss. Donors are expected to suppress the oxygen vacancy concentration and, thereby, the oxygen movement. The prediction is proven by niobium doping and found to be valid. The loss could be decreased in the entire temperature range of investigation.

In the absence of hydrogen, the formation of oxygen vacancies limits the stable operation of langasite resonators at fairly low oxygen partial pressures. The material shows increased *n*-type electronic conduction with decreasing oxygen partial pressure. Above e.g. 10^{-17}, 10^{-24} and 10^{-36} bar at 1000, 800 and 600 °C, respectively, the oxygen vacancy concentration remains almost constant and a stable resonance frequency is expected. In contrast, hydrogenous atmospheres cause a different behavior. The conductivity decreases with decreasing oxygen partial pressure. The incorporation

of OH-groups in oxygen vacancies results in a distinct correlation which is experimentally confirmed. Essentially, at low oxygen partial pressures the OH-groups are removed from the lattice which lowers the concentration of mobile hydrogen containing carriers and, thereby, the conductivity. The related frequency shift starts at higher oxygen partial pressures than in nominally hydrogen free atmospheres, i.e. below about 10^{-13} and 10^{-20} bar at 800 and 600°C, respectively. The frequency shift of langasite resonators is in accordance with conductivity changes which supports the model.

Application examples are summarized to demonstrate the capabilities of the high-temperature stable piezoelectric material. First, langasite based miniaturized structures are prepared. Thereby, the concept of monolithic electrodes is realized to reduce thermal stress. Heavily strontium doped langasite exhibits an increased conductivity by four orders of magnitude in comparison to nominally undoped langasite. Therefore, local strontium doping in the vicinity of the surface creates monolithic electrodes which are demonstrated to be operational up to 800°C. Langasite membranes are prepared by wet chemical etching. Thereby, 60 MHz membranes with a thickness of 23 μm show a mass sensitivity of 4.6 cm^2 Hz/ng. In addition, field emitter tips are realized and characterized at temperatures up to 600°C. The maximum field emission current is 67 μA. The minimum tip radius is calculated to be 27 nm. Finally, the simultaneous determination of mechanical and electrical properties of thin sensor films by an array of resonant sensors enables detection of CO in hydrogen containing atmospheres at 600°C.

Acknowledgements The contributions of the coworkers from Clausthal University of Technology, especially Dr. M. Schulz, Dr. D. Richter, J. Sauerwald and E. Ebeling, are highly acknowledged. Their experimental work and feedback helped substantially to broaden the knowledge about the high-temperature piezoelectric materials. Further, the author thanks Prof. G. Borchardt, Clausthal University of Technology, Dr. C. Rüscher, Leibniz University Hannover and Dr. H. Baumann, University of Frankfurt, for the support of the SIMS analysis, the FT-IR measurements and the gallium implantation, respectively. The tight collaboration with Prof. H.L. Tuller and Dr. H. Seh from Massachusetts Institute of Technology is one of the important driving forces of this work. Research grants from German Research Foundation (DFG) and German Government (BMBF) supported this work.

Appendix A: Crystal growth

Nominally undoped and doped langasite single crystals are prepared by the Institute for Crystal Growth, Berlin-Adlershof, Germany (IKZ Berlin) using the Czochralski technique [37]. Thereby, the starting powder is prepared by mixing stoichiometric amounts of La_2O_3, Ga_2O_3, and SiO_2 (purity 4N). After calcination, the material is charged into a crucible and heated. Subsequently, the crystals are pulled at a rate of 1.5 mm/h under N_2–2% O_2. Since the crystals are grown in iridium crucibles undoped material appears transparent independent of its treatment in oxidizing or reducing atmospheres. Intentionally doped langasite single crystals are also provided by IKZ Berlin. The growth process corresponds to that described above except for the partial replacement of lanthanum or gallium by the dopants, namely strontium, praseodymium and niobium.

Appendix B: Materials data

The bulk conductivity of the resonator materials is determined by impedance spectroscopy in the frequency range from 10 to 1 MHz. The low frequency intercept of the R_SC_S-semicircle in the complex impedance plane represents the resistance of the parallel arrangement and is converted in the bulk conductivity σ_R. Further,

Table 11 Room temperature materials constants of langasite, gallium phosphate and quartz

		Langasite		$GaPO_4$	Quartz
		[111]	[69]	[67, 68]	[44, 51]
ρ	[10^3 kg m^{-3}]	5.748		3.57	2.648
$\varepsilon_{11}/\varepsilon_0$		18.99		6.1	4.428
$\varepsilon_{33}/\varepsilon_0$		50.44		6.6	4.634
e_{11}	[C m^{-2}]	−0.436		0.209[a]	0.171
e_{14}		0.092		0.107[a]	0.041
c_{11}		18.924		6.658	8.674
c_{12}		10.489	10.33	2.181	0.699
c_{13}		9.782	9.71	2.487	1.191
c_{14}	[10^{10} Nm^{-2}]	1.448	1.50	0.391	1.791
c_{33}		26.330	26.19	10.213	10.720
c_{44}		5.343	5.33	3.766	5.794
c_{66}		4.232	4.28	2.238	3.988

[a]Calculated from $e_{ip} = d_{iq}c_{qp}$ [51]

the dielectric constant ε_R is extracted from the data. The resonance spectra of the piezoelectric resonators are determined by recording the real R and imaginary X parts of the impedance spectra in the vicinity of the resonance frequency using an high-speed network analyzer.

The fit procedure to determine the materials properties requires room-temperature data as initial values. They are taken from different publications and listed in Table 11. In addition, key values determined independently by pulse-echo measurements using the actual langasite crystals are given [69]. The high-temperature data of the piezoelectric material used for the parameter study correspond to some extend to those of langasite. The extrapolation up to 1400°C is done

- Linearly for the dielectric constant and the piezoelectric coefficient as given for 500, 1000 and 1400°C in Table 12,
- Parabolically for the shear modulus as given in Table 12,
- Exponentially for the conductivity and viscosity according to $\sigma_R T = \sigma_0 e^{-E_\sigma/k_B T}$ and $\eta_R = \eta_0 e^{-E_\eta/k_B T}$ as given in Figs. 6 and 10, respectively.

Appendix C: Diffusion coefficients

C.1 $^{16}O/^{18}O$ exchange

Self-diffusion coefficients can be extracted by analysis of the movements of stable tracers within a given sample. Oxygen diffusion measurements base commonly on the exchange of the stable tracer isotope ^{18}O with low natural abundance (0.206 at%), with that of naturally occurring ^{16}O in the solid.

In order to prepare the samples, pre-annealing runs are performed in artificial air at the same temperature and p_{O2} as the subsequent diffusion runs. Thereby, the period of time is chosen to be at least four times longer than that of the tracer diffusion. After pre-annealing, the samples are temporarily moved into a cooler area of the furnace ($\Delta T = 250$°C) to replace the gas atmosphere with $^{18}O_2$ enriched gas (typically 80–90%). The samples are then exposed to the tracer at temperatures ranging from 500 up to 1000°C to achieve the ^{18}O–^{16}O exchange. Subsequently, the resulting concentration profiles are determined by secondary ion mass spectrometry (SIMS, Cameca IMS 3f) or secondary neutral mass spectrometry (SNMS, VG SIMS Lab).

The ^{18}O concentration at the surface of the sample c_S is potentially lower than the concentration in the surrounding gas environment c_G. Therefore, the surface exchange kinetics must be taken into consideration.

Table 12 Material constants used for the parameter study at elevated temperatures

Temperature [°C]	ε_R [10^{-10}]	η_R [Pa s]	e_R [Cm^{-2}]	c_{66} [10^{10} Nm^{-2}]
500	2.02	1.14	0.52	4.11
1000	2.33	2.57	0.61	3.87
1400	2.54	3.47	0.67	3.58

C.2 Diffusion in single crystals

The diffusion model given in [112] describes the such situations for a single diffusion mechanism. Here, the surface exchange kinetics and the bulk diffusion are expressed by k and D, respectively

$$k\,(c_G - c_S) = D\frac{\partial c}{\partial y}\bigg|_{y=0}. \tag{73}$$

The measured depth profiles are fitted by a least square regression procedure based upon the diffusion solution according to Eq. 74

$$\frac{c(y,t)-c_{BG}}{c_G-c_{BG}} = \operatorname{erfc}\left(\frac{y}{2\sqrt{Dt}}\right) - \exp\left(\frac{k}{D}y+\frac{k^2}{D}t\right) \times \operatorname{erfc}\left(\frac{y}{2\sqrt{Dt}}+k\sqrt{\frac{t}{D}}\right) \tag{74}$$

where y, t and c_{BG} are the depth, the diffusion time and the natural background ^{18}O concentration, respectively.

C.3 Diffusion in polycrystalline materials

The analytical solution in the form of Eq. 74 cannot be applied if more than one diffusion mechanism takes place simultaneously. For example, polycrystalline samples exhibit diffusion in the volume and the grain boundaries. The common way to plot the corresponding diffusion profiles is to express the logarithm of the concentration as a function of depth to the power of 6/5. The grain boundary term is then visible as the linear part of the concentration profile, and from the slope the grain boundary diffusion coefficient can be calculated [113] when the volume diffusion coefficient is known. In this study, the analytical approach proposed in [114] is used. The linear part of the depth profile, plotted versus $x^{6/5}$ and extrapolated to $x = 0$, represents the contribution of grain boundaries, c^0_{GB}, approximated by

$$c^0_{GB} = 0.9\,c_G\lambda\,2\sqrt{Dt}. \tag{75}$$

Here, λ and D are the grain boundary length per unit area and the bulk diffusion coefficient, respectively. The grain boundary length may be extracted by processing cross sections of the specimen. Examples for diffusion profiles and cross sections of the specimen are given in [115]. A typical grain boundary length per unit area is $\lambda = (0.7 \pm 0.1)\ \mu m^{-1}$.

C.4 Ion implantation

The determination of the gallium diffusion coefficients can be performed using the stable isotope ^{71}Ga. The small difference in abundance of the gallium isotopes ^{69}Ga and ^{71}Ga (61 and 39 at%, respectively) requires the application of large quantities of ^{71}Ga. Nevertheless, a poor signal resolution during analysis has to be expected.

The isotope ^{71}Ga is implanted into the specimens at the University of Frankfurt, Germany. The tracer, extracted from a gallium arsenate plasma, is accelerated to 50 keV and focused on the surface of *y*-cut langasite plates. The total amount of implanted ^{71}Ga ions is about 8×10^{16} ions/cm^2. To avoid electrical charging of the surface, the samples are treated with an additional electron beam. The subsequent diffusion runs are performed in air at temperatures from 700 up to 1000°C.

^{71}Ga is implanted by a 50 keV accelerator. Damage of the lattice in the implanted region is, therefore, expected and the evaluation of the diffusion coefficients must account for the damaged region. Fick's second law still describes the transport. But the equation has to be solved numerically by e.g. using the Crank-Nicolson scheme [116]. Details are presented in [115].

References

1. M. Pereira da Cunha, R.J. Lad, T. Moonlight, G. Bernhardt, D.J. Frankel, in *High Temperature Stability of Langasite Surface Acoustic Wave Devices*. Proc. IEEE Int. Ultras. Symp. (2008), pp. 205–208
2. I. Shrena, D. Eisele, E. Mayer, L.M. Reindl, J. Bardong, M. Schmitt, *SAW-Relevant Material Properties of Langasite in the Temperature Range from 25 to 750°C: New Experimental Results*. Proc. IEEE Int. Ultras. Symp. (2008), pp. 209–212
3. H. Fritze, High-temperature bulk acoustic wave sensors. Meas. Sci. Technol. **22**, 12002 (2011). 28 pp
4. O. Knacke, O. Kubaschewski, H. Hesselmann, *Thermochemical Properties of Inorganic Substances* (Springer, New York, 1991)
5. R.W. Cernosek, J.R. Bigbie, M.T. Anderson, J.H. Small, P.S. Sawyer, in *High Temperature Hydrocarbon Gas Sensing with Mesoporous SiO_2 Thin Films on TSM Resonators*. Solid-State Sensor and Actuator Workshop, Hilton Head Island, South Carolina, 8–11 November 1998
6. D. Damjanovic, Materials for high temperature piezoelectric transducers. Curr. Opin. Solid State Mater. Sci. **3**, 469–473 (1998)
7. L. Reindl, G. Scholl, T. Ostertag, H. Scherr, U. Wolff, F. Schmidt, Theory and application of passive SAW radio transponder as sensors. IEEE Trans. Ultrason. Ferroelectr. Freq. Control **45**, 1281–1292 (1998)
8. R. Fachberger, G. Bruckner, G. Knoll, R. Hauser, J. Biniasch, L. Reindl, Applicability of $LiNbO_3$, langasite and $GaPO_4$ in high temperature SAW sensors operating at radio frequencies. IEEE Trans. Ultrason. Ferroelectr. Freq. Control **51**(11), 1427–1431 (2004)
9. D.P. Birnie III, Analysis of diffusion in lithium niobate. J. Mater. Sci. **28**, 302–315 (1993)
10. M. Strassburg, J. Senawiratne, N. Dietz, U. Haboeck, A. Hoffmann, V. Noveski, R. Dalmau, R. Schlesser, Z. Sitar, The growth and optical properties of large, high-quality AlN single crystals. J. Appl. Phys. **6**, 5870–5876 (2004)
11. A.D. Katnani, K.I. Papathomas, Kinetics and initial stages of oxidation of aluminum nitride: thermogravimetric analysis and x-ray photoelectron spectroscopy study. J. Vac. Sci. Technol. **A5**, 1335–1340 (1987)
12. A. Bellosi, E. Landi, A. Tampieri, Oxidation behavior of aluminum nitride. J. Mater. Res. **8**, 565–572 (1993)
13. O. Ambacher, M.S. Brandt, R. Dimitrov, R.A. Fischer, A. Miehr, T. Metzger, M. Stutzmann, Thermal stability and desorption of group III nitrides prepared by MOCVD. J. Vac. Sci. Technol. **14**, 3532–3542 (1996)
14. K. Shimamura, H. Takeda, T. Kohno, T. Fukuda, Growth and characterization of lanthanum gallium silicate $La_3Ga_5SiO_{14}$ single crystals for piezoelectric applications. J. Cryst. Growth **163**, 388–392 (1996)
15. B. Chai, J.L. Lefaucheur, Y.Y. Ji, H. Qiu, in *Growth and Evaluation of Large Size LGS ($La_3Ga_5SiO_{14}$), LGN ($La_3Ga_{5,5}Nb_{0,5}O_{14}$) and LGT ($La_3Ga_{5,5}Ta_{0,5}O_{14}$) Single Crystals*. IEEE Int. Freq. Contr. Symp. (1998), pp. 748–760
16. P.W. Krempl, Quartzhomeotypic gallium orthophosphate: a new high tech piezoelectric crystal. Ferroelectrics **202**, 65–69 (1997)
17. K. Jacobs, P. Hofmann, D. Klimm, J. Reichow, M. Schneider, Structural phase transformations in crystalline gallium orthophosphate. J. Solid State Chem. **149**, 180–188 (2000)
18. F. Krispel, C. Reiter, J. Neubig, F. Lenzenhuber, P.W. Krempl, W. Wallnöfer, P.M. Worsch, in *Properties and Applications of Singly Rotated $GaPO_4$ Resonators*. IEEE Int. Freq. Contr. Symp. (2003), pp. 668–673
19. S. Uda, S.Q. Wang, N. Konishi, H. Inaba, J. Harada, Growth habits of 3 and 4-inch langasite single crystals. J. Cryst. Growth **237–239**, 707–713 (2002)
20. P. Krempl, G. Schleinzer, W. Wallnöfer, Gallium phosphate, $GaPO_4$: a new piezoelectric crystal material for high-temperature sensorics. Sens. Actuators, A **61**, 361–363 (1997)
21. F. Krispel, H. Thanner, P. Krempl, C. Reiter, P. Worsch, W. Wallnöfer, in *$GaP0_4$ Resonators With Q Factors of Some Millions in the Fundamental Mode*. IEEE International Frequency Control Symposium (2002), pp. 342–346
22. H. Fritze, O. Schneider, G. Borchardt, in *High Temperature Bulk Acoustic Wave Properties of Gallium Orthophosphate and Langasite*, Sensor 2003 Proceedings, (AMA Service GmbH) (2003)
23. K. Jacobs, P. Hofmann, D. Klimm, OH impurities in $GaPO_4$ crystals: correlation between infrared absorption and mass loss during thermal treatment. J. Cryst. Growth **237–239**, 837–842 (2002)

24. R.-U. Barz, M. Grassl, P. Gille, Study of anisotropic effects in hydrothermal growth of gallium orthophosphate single crystals. Ann. Chim. Sci. Mat. **26**, 95–98 (2001)
25. K. Jacobs, P. Hofmann, J. Reichow, Physico-chemical aspects of the hydrothermal growth of $GaPO_4$. Ann. Chim. Sci. Mat. **26**, 85–90 (2001)
26. O. Cambon, P. Yot, D. Balitsky, A. Goiffon, E. Philippot, B. Capelle, J. Detaint, Crystal growth of $GaPO_4$, a very promising material for manufacturing BAW devices. Ann. Chim. Sci. Mat. **26**, 79–84 (2001)
27. S. Zhang, Y. Fei, B.H.T. Chai, E. Frantz, D.W. Snyder, X. Jiang, T.R. Shrout, Characterization of piezoelectric single crystal $YCa_4O(BO_3)_3$ for high temperature applications. Appl. Phys. Lett. **92**, 202905 (2008)
28. S. Zhang, E. Frantz, R. Xia, W. Everson, J. Randi, D.W. Snyder, T.R. Shrout, Gadolinium calcium oxyborate piezoelectric single crystals for ultrahigh temperature (>1000°C) applications. J. Appl. Phys. **104**, 084103 (2008)
29. F. Yu, S. Zhang, X. Zhao, D. Yuan, Q. Wang, T.R. Shrout, High temperature piezoelectric properties of yttrium calcium oxyborate single crystals. Phys. Status Solidi - RRL **4**, 103–105 (2010)
30. D. Cachau-Herreillat, J. Bennazha, A. Goiffon, A. Ibanez, E. Philippot, X-ray, DTA and crystal growth investigation on $AlPO_4$-$GaPO_4$ and $AlPO_4$-$AlAsO_4$ systems. Eur. J. Solid State Inorg. Chem. **29**, 1295–1307 (1992)
31. H. Fritze, High temperature piezoelectric materials: Defect chemistry and electro-mechanical properties. J. Electroceramics **17**, 625–630 (2006)
32. J. Sauerwald, H. Fritze, E. Ansorge, S. Schimpf, S. Hirsch, B. Schmidt, in *Electromechanical Properties of Langasite Structures at High Temperatures*. International Workshop on Integrated Electroceramic Functional Structures, Berchtesgaden, Germany, 6–8 June 2005
33. B.V. Mill, Y.V. Pisarevsky, in *Langasite-type Materials: From Dicovery to Present State*. Proc. IEEE/EIA Int. Freq. Control Symp. (2000), pp. 133–144.
34. A.N. Gotalskaya, D.I. Drezin, V.V. Bezdelkin, V.N. Stassevich, in *Pecularities of Technology, Physical Properties and Applications of New Piezoelectric Material Langasite* ($La_3Ga_5SiO_{14}$). IEEE Int. Freq. Contr. Symp. (1993), pp. 339–347.
35. J. Bohm, E. Chilla, C. Flannery, H.-J. Fröhlich, T. Hauke, R. Heimann, M. Hengst, U. Straube, Czochralski growth and characterization of piezoelectric single crystals with langasite structure: LGS, LGN and LGT. Part II: Piezoelectric and elastic properties. J. Cryst. Growth **216**, 293–298 (2000)
36. J. Boy, R. Besson, E. Bigler, R. Bourquin, B. Dulmet, in *Theoretical and Experimental Studies of the Force-Frequency Effect in BAW LGS and LGT Resonators*. IEEE Int. Freq. Contr. Symp. (2001), pp. 223–226
37. S. Ganschow, C. Cavalloni, P. Reiche, R. Uecker, Growth of $La_3Ga_5SiO_{14}$: a modern material for high-temperature piezoelectric application. Proc. SPIE **2373**, 55–58 (1995)
38. H. Takeda, S. Tanaka, S. Izukawa, H. Shimizu, T. Nishida, T. Shiosaki, in *Effective Substitution of Aluminum for Gallium in Langasite-type Crystals for A Pressure Sensor Use at High Temperature*. IEEE Ultras. Symp. (2005), pp. 560–563
39. E.N. Domoroshchina, A.B. Dubovskii, G.M. Kuz'micheva, G.V. Semenkovich, Influence of point defects on the electrical conductivity and dielectric properties of langasite. Inorg. Mater. **41**, 1378–1381 (2005)
40. H. Fritze, H.L. Tuller, G. Borchardt, T. Fukuda, High temperature properties of langasite. Mater. Res. Soc. Symp. Proc. **604**, 65–70 (2000)
41. H. Fritze, H.L. Tuller, Langasite for high temperature bulk acoustic wave applications. Appl. Phys. Lett. **78**, 976–977 (2001)
42. H. Fritze, H. Seh, H.L. Tuller, G. Borchardt, Operation limits of langasite high temperature nanobalances. J. Eur. Ceram. Soc. **21**, 1473–1477 (2001)
43. J. Stade, L. Bohaty, M. Hengst, R.B. Heimann, Electro-optic, piezoelectric and dielectric properties of langasite ($La_3Ga_5SiO_{14}$), langanite ($La_3Ga_{5.5}Nb_{0.5}O_{14}$) and langataite ($La_3Ga_{5.5}Ta_{0.5}O_{14}$). Cryst. Res. Technol. **37**, 1113–1120 (2002)
44. D.R. Lide (ed.), *CRC Handbook of Chemistry and Physics*, 84th edn. (CRC Press, Boca Raton, 2003)
45. C. Klemenz, M. Berkowski, B. Deveaud-Pledran, D.C. Malocha, in *Defect Structure of Langasite-type Crystals: A Challange for Applications*. IEEE Int. Freq. Contr. Symp. (2002), pp. 301–306
46. R. Fachberger, E. Riha, E. Born, W. Ruile, P. Pongratz, S. Kronholz, in *Homogeneity of Langasite and Langatate Wafers*. IEEE Int. Freq. Contr. Symp. (2002), pp. 311–319
47. G.M. Kuz'micheva, V.B. Rybakov, E.N. Domoroshchina, A.B. Dubovskii, X-ray diffraction study of an inhomogeneous langasite ($La_3Ga_5SiO_{14}$) crystal. Inorg. Mater. **38**, 1040–1047 (2002)
48. G. Sauerbrey, Verwendung von Schwingquarzen zur Wägung dünner Schichten und zur Mikrowägung. Z. Phys. **155**, 206–222 (1959)
49. E. Benes, Improved quartz microbalance technique. J. Appl. Phys. **56**, 608–626 (1984)
50. S.S. Narine, A.J. Slavin, Use of the quartz crystal microbalance to measure the mass of submonolayer deposits: Measuring the stoichiometry of surface oxides. J. Vac. Sci. Technol. **A16**, 1857–1862 (1998)
51. IEEE Standard on Piezoelectricity, ANSI/IEEE Std. 176-1987 (The Institute of Electrical and Electronic Engineers, New York, 1988)
52. D.A. Berlincourt, D. Curran, H. Jaffe, in *Physical Acoustics, Principles and Methods*. Piezoelectric and Piezomagnetic Materials and their Function in Transducers, vol. 1, part A. (Academic, New York, 1964), Ch. 3, pp. 169–270
53. T. Ikeda, *Fundamentals of Piezoelectricity* (Oxford University Press, Oxford, 1990)
54. J. Vig, Quartz crystal resonators and oscillators (2001). www.ieee-uffc.org/freqcontrol/tutorials/. Accessed 8 June 2001
55. D. Salt, *Hy-Q Handbook of Quartz Crystal Devices* (Van Nostrand Reinhold, Wokingham, 1987)
56. B. Zimmermann, R. Lucklum, P. Hauptmann, J. Rabe, S. Büttgenbach, Electrical characterisation of high-frequency thickness shear-mode resonators by impedance analysis. Sens. Actuators, B **76**, 47–57 (2001)
57. K.W. Kwok, H.L.W. Chan, C.L. Choy, Evaluation of the material parameters of piezoelectric materials by various methods. IEEE Trans. Ultrason. Ferroelectr. Freq. Control **44**(4), 733–742 (1997)
58. J.G. Smith, Influence of moving domain walls and jumping lattice defects on complex material coefficients of piezoelectrics. IEEE Trans. Sonics Ultrason. **SU-23**(3), 168–174 (1976)
59. G. Arlt, The role of domain walls on the dielectric, elastic and piezoelectric properties of ferroelectric ceramics. Ferroelectrics **76**, 451–458 (1987)
60. W. Göpel, J. Hesse, J.N. Zehmel, *Sensors, a comprehensive survey*, vol. 7 (VCH, Weinheim, 1994)
61. H.F. Tiersten, *Linear Piezoelectric Plate Vibration* (Plenum, New York, 1969)

62. H. Fritze, M. Schulz, H. Seh, H.L. Tuller, Sensor application-related defect chemistry and electromechanical properties of langasite. Solid State Ion. **177**, 2313–2316 (2006)
63. B.A. Martin, H.E. Hager, Velocity profile on quartz crystals oscillating in liquids. J. Appl. Phys. **65**, 2630–2635 (1989)
64. G. Sauerbrey, Messung von Plattenschwingungen sehr kleiner Amplitude durch Lichtmodulation. Z. Phys. **178**, 457–471 (1964)
65. J. Schreuer, J. Rupp, C. Thybaut, J. Stade, in *Temperature Dependence of Elastic, Piezoelectric and Dielectric Properties of $La_3Ga_5SiO_{14}$ and $La_3Ga_{5.5}Ta_{0.5}O_{14}$: An Application of Resonant Ultrasound Spectroscopy*. IEEE Ultras. Symp. (2002), pp. 360–363
66. T. Schneider, S. Doerner, P. Hauptmann, H. Fritze, D. Richter, Novel impedance interface for resonant high-temperature gas sensors. Sens. Actuators, B **111–112**, 187–192 (2005)
67. C. Reiter, P.W. Krempl, H. Thanner, W. Wallnöfer, P.M. Worsch, Material properties of GaPO4 and their relevance for application. Ann. Chim. Sci. Mat. **26**, 91–94 (2001)
68. Piezocryst GmbH, Data sheet: $GaPO_4$ material constants, Update 11/2005 (2001). http://www.piezocryst.com. Accessed 14 August 2001
69. M. Schulz, H. Fritze, U. Straube, in *Determination of Material Parameters of Langasite ($La_3Ga_5SiO_{14}$) at Elevated Temperatures*. 345th Wilhelm and Else Heraeus Seminar: "Acoustic Wave Based Sensors: Fundamentals, Concepts, New Applications," Bad Honnef, Germany, 11–13 April 2005
70. M. Schulz, Untersuchung der Eigenschaften von Langasit für Hochtemperaturanwendungen, Ph.D. thesis, Technische Unversität Clausthal, 2007
71. J.J. Martin, in *Acoustic Loss in Cultured Quartz*. IEEE Int. Freq. Contr. Symp. (1996), pp. 170–178
72. J.J. Martin, in *High-temperature Acoustic Loss In Thickness-Shear Mode Quartz Resonators*. IEEE/EIA Int. Freq. Contr. Symp. (2000), pp. 359–363
73. T. Norby, Solid-state protonic conductors: principles, properties, progress and prospects. Solid State Ion. **125**, 1–11 (1999)
74. J. Crank, *The Mathematics of Diffusion* (Oxford University Press, Oxford, 1975)
75. T. Ishihara, H. Matsuda, Y. Takita, Oxide ion conductivity in doped $NdAlO_3$ perovskite-type oxides. J. Electrochem. Soc. **141**, 3444–3449 (1994)
76. N.J. Long, F. Lecarpentier, H.L. Tuller, Structure and electrical properties of Ni-substituted lanthanum gallate perovskites. J. Electroceram. **3**(4), 399–407 (1999)
77. C. Klemenz, High-quality $La_3Ga_{5.5}Ta_{0.5}O_{14}$ and $La_3Ga_{5.5}Nb_{0.5}O_{14}$ LPE films for oscillators and resonators. J. Cryst. Growth **250**, 34–40 (2003)
78. D.P. Butt, Y. Park, T.N. Taylor, Thermal vaporization and deposition of gallium oxide in hydrogen. J. Nucl. Mater. **264**, 71–77 (1999)
79. B.A. Maksimov, S.S. Kazantsev, V.N. Molchanov, I.A. Verin, B.V. Mill, Crystal structure and microtwinning of monoclinic $La_3SbZn_3Ge_2O_{14}$ crystals of the langasite family. Crystallogr. Rep. **49**, 585–590 (2004)
80. H. Seh, H.L. Tuller, Defects and transport in langasite I: acceptor-doped ($La_3Ga_5SiO_{14}$). J. Electroceram. **16**, 115–125 (2006)
81. H. Seh, H.L. Tuller, Defects and transport in langasite II: donor-doped $La_3Ga_{4.75}Nb_{0.25}SiO_{14}$. J. Electroceramics **15**, 192–202 (2005)
82. H. Seh, H. Fritze, H.L. Tuller, Defect chemistry of langasite III: predictions of electrical and gravimetric properties and application to operation of high temperature crystal microbalance. J. Electroceramics **18**, 130–147 (2007)
83. H. Seh, Langasite bulk acoustic wave resonant sensor for high temperature applications. Ph.D. thesis, Department of Materials Science and Engineering, MIT, Cambridge, MA, USA, 2005
84. K. Schulgasser, Relationship between single-crystal and polycrystal electrical conductivity. J. Appl. Phys. **47**, 1880–1886 (1976)
85. H. Kimura, S. Uda, X. Huang, S. Koh, in *Equilibrium Phase diagram of Incongruent-Melting Langatate ($La_3Ta_{0.5}Ga_{5.5}O_{14}$) and the Influence of Growth Atmosphere and Impurity Ir on the Resistivity of Langatate*. 15th International Conference on Crystal Growth, Salt Lake City, USA, 12–17 August 2007 (preliminary abstract: http://www.crystalgrowth.us/iccg15)
86. P.G. Shewmon, *Diffusion in Solids* (McGraw-Hill, New York, 1963)
87. J. Maier, Mass transport in the presence of internal defect reactions-concept of conservative ensembles: IV tracer diffusion and intercorrelation with chemical diffusion and ion conductivity. J. Am. Ceram. Soc. **76**, 1228–1232 (1993)
88. A. Kaminskii, B. Mill, G. Khodzhabagyan, A. Konstantinova, O.A.I., I. Silvestrova, Investigation of trigonal $(La_{1-x}Nd_x)_3Ga_5SiO_{14}$ crystals: I. Growth and optical properties. Phys. Stat. Sol. (A) **80**, 387–398 (1983)
89. I.H. Jung, Y.H. Kang, K. Joo, A. Yoshikawa, T. Fukuda, K. Auh, $Ca_3Ga_2Ge_4O_{14}$ (CGG)-type $Sr_3Nb_{0.95}Ga_{3.083}Si_2O_{14}$ single crystal grown by the Czochralski method for piezoelectric applications. Mater. Lett. **51**, 129–134 (2001)
90. B.H.T. Chai, A.N.P. Bustamante, M.C. Chou, in *A New Class of Ordered Langasite Structure Compounds*. IEEE/EIA Int. Freq. Contr. Symp. (2000), pp. 163–168
91. F.A. Kröger, *The Chemistry of Imperfect Crystals* (North Holland, Amsterdam, 1964)
92. Y.-M. Chiang, D.P. Birnie III, W.D. Kingery, *Physical Ceramics* (Wiley, New York, 1996)
93. R.H. Doremus, *Diffusion of Reactive Molecules in Solids and Melts* (Wiley, New York, 2002)
94. R. Glöckner, A. Neiman, Y. Larring, T. Norby, Protons in $Sr_3(Sr_{1+x}Nb_{2-x})O_{9-3x/2}$ perovskite. Solid State Ion. **125**, 369–376 (1999)
95. S. Suzuki, S. Nakashima, In-situ IR measurements of OH species in quartz at high temperatures. Phys. Chem. Miner. **26**, 217–225 (1999)
96. F. Shimojo, K. Hoshino, H. Okazaki, Effects of doped acceptor ions on proton diffusion in perovskite oxides: a first-principles molecular dynamics simulation. J. Phys.: Condens. Matter **10**, 285–294 (1998)
97. I.E. Animitsa, A.Y. Neiman, A.R. Sharafutdinov, M.G. Kazakova, Strontium tantalates with a perovskite structure: their conductivity and high-temperature interaction with water. Russ. J. Electrochem. **37**, 266–272 (2001)
98. J. Schreuer, C. Thybaut, M. Prestat, J. Stade, E. Haussuhl, in *Towards an Understanding of the Anomalous Electromechanical Behaviour of Langasite and Related Compounds at High Temperatures*. IEEE Ultras. Symp. (2003), pp. 196–199
99. W. Johnson, S. Kim, S. Uda, in *Acoustic Loss in Langasite and Langanite*. Proc. IEEE Int. Freq. Contr. Symp. (2003), pp. 646–649

100. E. Ansorge, S. Schimpf, S. Hirsch, J. Sauerwald, H. Fritze, B. Schmidt, Evaluation of langasite ($La_3Ga_5SiO_{14}$) as a material for high temperature microsystems. Sens. Actuators A **130–131**, 393–396 (2006)
101. E. Ansorge, B. Schmidt, J. Sauerwald, H. Fritze, Langasite for microelectro-mechanical systems. Phys. Status Solidi A **208**, 377–389 (2011)
102. J. Sauerwald, D. Richter, H. Fritze, Micromachined piezoelectric structures for high-temperature sensors. J. Electroceramics **22**, 180–184 (2009)
103. J. Sauerwald, D. Richter, E. Ansorge, B. Schmidt, H. Fritze, Langasite based miniaturized functional structures—preparation, high-temperature properties and applications. Phys. Status Solidi A **208**, 390–403 (2011)
104. H. Fritze, O. Schneider, H. Seh, H.L. Tuller, G. Borchardt, High temperature bulk acoustic wave properties of langasite. Phys. Chem. Chem. Phys. **5**, 5207–5214 (2003)
105. S.L. Firebaugh, K.F. Jensen, M.A. Schmidt, Investigation of high-temperature degradation of platinum thin films with an in-situ resistance measurement apparatus. J. Microelectromech. Syst. **7**, 128–135 (1998)
106. K. Inoue, S. Katsuo, Propagation characteristics of surface acoustic waves on langasite. Jpn. J. Appl. Phys. **37**, 2909–2913 (1998)
107. R. Fowler, L. Nordheim, Electron emission in intense electric fields. Proc. R. Soc. Lond. A-Contain Pap. Biol. Character **119**, 173–181 (1928)
108. C.A. Spindt, I. Brodie, L. Humphrey, E.R. Westerberg, Physical properties of thin-film field emission cathodes with molybdenum cones. J. Appl. Phys. **47**, 5248–5263 (1976)
109. H. Fritze, H.L. Tuller, Erfassen eines Umwelteinflusses durch Änderung der Leitfähigkeit der Sensorschicht eines piezoelektrischen Materials Europäisches Patent Nr. 1695074
110. D. Richter, H. Fritze, T. Schneider, P. Hauptmann, in *Selectivity Improvement of High Temperature Resonant Gas Sensors by Application of Different Electrode Layouts*. Sensor, Internat. Conf. (Wunstorf: AMA Service), vol. 12, pp. 19–24 (2005)
111. J.A. Kosinski, R.A. Pastore, Jr., E. Bigler, M. Pereira da Cunha, C.D. Malocha, J. Detaint, in *A Review of Langasite Material Constants from BAW and SAW Data: Toward an Improved Data Set*. IEEE Int. Freq. Contr. Symp. (2001), pp. 278–286
112. J.A. Kilner, R.A. De Souza, I.C. Fullarton, Surface exchange of oxygen in mixed conducting perovskite oxides. Solid State Ion. **86–88**, 703–709 (1996)
113. A.D. Le Claire, The analysis of grain boundary diffusion measurement. Br. J. Appl. Phys. **14**, 351–356 (1963)
114. P. Fielitz, G. Borchardt, M. Schmücker, H. Schneider, How to measure volume diffusivities and grain boundary diffusivities of oxygen in polycrystalline oxides. Solid State Ion. **160**, 75–83 (2003)
115. M. Schulz, H. Fritze, H.L. Tuller, H. Seh, Diffusion related implications for langasite resonator operation. IEEE Trans. Ultrason. Ferroelectr. Freq. Control **51/11**, 1381–1387 (2004)
116. W.H. Press, B.P. Flannery, S.A. Teukolsky, W.T. Vetterling, *Numerical Recipes in Pascal*. (Cambridge University Press, New York, 1994)